Charles University in Prague
Faculty of Science

Department of Physical and Macromolecular Chemistry
Study branch: Physical chemistry

Bc. Karel Šindelka

Self-assembly of polyelectrolytes in aqueous solutions (dissipave particle dynamics)

Spontánní asociace polyelektrolytů ve vodných roztocích (disipativní částicová dynamika)

Diploma thesis

Supervisor: Doc. Ing. Zuzana Limpouchová, CSc.
Consultant: Doc. Ing. Martin Lísal, DSc.

Prague, 2014

I would like to express my sincere thanks to all my research group members, especially to my supervisor Zuzana Limpouchová for her support and great patience – without it this work would never be possible. I am also grateful to my co-supervisor Martin Lísal and Karel Procházka for their invaluable help. Last but not least I wish to thank Ave, my family and friends for their support.

Prohlášení

Prohlašuji, že jsem závěrečnou práci zpracoval samostatně a že jsem uvedl všechny použité informační zdroje a literaturu. Tato práce ani její podstatná část nebyla předložena k získání jiného nebo stejného akademického titulu.

V Praze 13. 5. 2014 Karel Šindelka

Contents

Title: Self-assembly of polyelectrolytes in aqueous solutions (dissipative particle dynamics)
Author: Karel Šindelka
Department: Faculty of science, Charles University in Prague
Supervisor: Doc. Ing. Zuzana Limpouchová, CSc.
Consultant: Doc. Ing. Martin Lísal, DSc.

Abstract

In the thesis, the coarse-grained dissipative particle dynamics (DPD) is used for the study of self-assembly of equimolar mixtures of oppositely charged symmetric block PEs with one PE block (either strong polycation or strong polyanion) and one readily water-soluble neutral block in aqueous media.

In the first part of the diploma thesis, the principles of DPD simulations are described and the correct implementation of electrostatic interactions in the DPD method is demonstrated on the example of counterion (Manning) condensation.

In the second main part, the effect of the blocks solubility, incompatibility and the interplay of different forces on electrostatic assembly is investigated. The corresponding neutral systems are also simulated for comparison. The study shows that the hydrophobicity of the PE backbone and the incompatibility of blocks significantly affects the electrsotatic co-assembly. The presence of opposite charges on different chains promotes the aggregation process and the aggregation number increases in comparison with the corresponding neutral system. In systems with well soluble charged blocks, only dimers are formed, while in systems with hydrophobic charged blocks, core-shell aggregates are formed for incompatible blocks and nano-gel particles for compatible blocks.

Keywords: polyelectrolytes, block copolymers, computer simulations

Název: Spontánní asociace (dissipative particle dynamics)
Autor: Karel Šindelka
Ústav: Faculty of science, Charles University in Prague
Školitel: Doc. Ing. Zuzana Limpouchová, CSc.
Konzultant: Doc. Ing. Martin Lísal, DSc.

Abstrakt

V diplomové práci je studována spontánní asociace ekvimolární směsi kladně a záporně nabitých symetrických blokových kopolymerů s jedním polyelektrolytovým blokem (silný polykation nebo silný polyanion) a jedním dobře rozpustným blokem ve vodných roztocích pomocí zhrubeného modelu a disipativní částicové dynamiky (DPD).

V první části diplomové práce jsou popsány základy DPD simulací a správnost implementace elektrostatických interakcí do DPD metody je ukázána na příkladu kondenzace protiiontů (Manningovy kondenzace).

Ve druhé stěžejní části je studován vliv rozpustnosti obou bloků, jejich nekompatibility a vzájemné souhry různých sil na elektrostatickou asociaci. Pro srovnání jsou uvedeny také simulace odpovídajících neutrálních systémů. DPD studie ukázala, že jak rozpustnost polyelektrolytového bloku tak nekompatibilita bloků hrají při elektrostatické asociaci důležitou roli. Přítomnost opačných nábojů na různých řetězcích přispívá k agregaci a vede k vyššímu agregačnímu číslu ve srovnání s odpovídajícím neutrálním systémem. V systémech s dobře rozpustným nabitým blokem vznikají pouze dimery, zatímco v systémech se špatně rozpustným polyelektrolytovým blokem vznikají agregáty s jádrem a slupkou pro nekompatibilní bloky a nanogelové částice pro kompatibilní bloky.

Klíčová slova: polyelektrolyty, blokové kopolymery, počítačové simulace

List of symbols and abbreviations

ξ	Manning parameter
l_{B}	Bjerrum length
l	polymer contour length containing elementary charge
e	electron charge
k_{B}	Boltzmann's constant
ϵ_0, ϵ_{r}	dielectric constants
T	temperature
$\mathbf{f}_i$	force acting on the i-th particle
m_i	mass of the i-th particle
$\mathbf{v}_i$	velocity vector of the i-th particle
$\mathbf{r}_i$	position vector of the i-th particle
t	time
$\mathbf{F}_{ij}^{\mathrm{C}}$	conservative force between particles i and j
$\mathbf{F}_{ij}^{\mathrm{D}}$	dissipative force between particles i and j
$\mathbf{F}_{ij}^{\mathrm{R}}$	random force between particles i and j
r_{c}	cut-off distance
U^{C}	soft repulsive potential
a_{ij}	repulsion coefficient between particles i and j
r_{ij}	distance between particles i and j
$\mathbf{e}_{ij}$	unit vector in a direction of particles' separation
ω^{D}	weight function for dissipative force
γ_{ij}	friction coefficient
ω^{R}	weight function for random force
σ_{ij}	noise amplitude
ζ_{ij}	Gaussian random number
Δt	simulation timestep
ρ	particle number density
χ_{ij}	Flory-Huggins parameter
α_ρ	proportionality constant
δ_i	solubility parameter

V_{DPD}	volume of a single DPD bead
$\mathbf{F}^{\mathrm{S}}_{i,i+1}$	spring force between two adjacent beads i and $i+1$
k_{s}	spring constant
r_0	equilibrium distance
N	total number of particles
q_i	charge of i-th particle
L	side length of a cubic simulation box
V	volume of a simulation box
U^{el}	electrostatic potential
$\mathbf{m}$, $\mathbf{n}$	integer vectors in Ewald sum
α	convergence parameter in Ewald sum
$\mathbf{k}$, k	reciprocal vector and its magnitude
ρ_{c}	charge density
r_{e}	smearing radius for linear charge density
σ	size of a Gaussian charge cloud
λ_{e}	decay length for Slater-type charge density
U^{el}_{ij}	electrostatic potential with smeared charge
β	electrostatic smearing constant
F^{el}_{ij}	electrostatic force with smeared charge
N_{m}	number of molecules in one DPD particle
C_{n}	number of monomers in one Kuhn segment
A_{s}	aggregation number
F_{w}	weight distribution function
F_{n}	number distribution function
n_{DPD}	number of physical monomers in one DPD bead
M	molar mass
τ	relaxation time
R_{g}	radius of gyration
$\mathbf{r}_{\mathrm{CM}}$	position vector of the center of mass of a chain or an aggragate
$\mathbf{S}$	gyration tensor
λ_x^2, λ_y^2, λ_z^2	eigenvalues of the gyration tensor
b	asphericity

c	acylindricity
κ^2	relative shape anisotropy
g	radial distribution function

PE	polyelectrolyte
MD	molecular dynamics
DPD	dissipative particle dynamics
erfc	complimentary error function
ACF	autocorrelation function

1. Introduction

Polymers play an important role in everyday life of the human society. Synthetic polymers are very prominent and widespread materials. Biopolymers are an important component of biological structures.

Polymer is a molecule consisting of many repeating structural units called monomers, which are connected by covalent bonds to form a chain. The number of monomers in one chain is called the degree of polymerization. Polymer chain can consist of only one type of monomer unit (homopolymer) or more types (copolymer). The two (or more) monomer types in the copolymer can be arranged for example to alternate regularly or to form blocks, where only one monomer type is present. Another important characteristic of polymer structure is chain architecture: linear, star-branched, H-branched, comb, dendrimer, etc. Due to the polymer chain's flexibility it can adopt many different conformations, making it practically impossible to describe its properties without the use of statistical approaches.

The conformation of the polymer chain in solution greatly depends on its interactions with a solvent [1, 2, 3]. If the interactions are favourable, the solvent is called thermodynamically good solvent and the polymer dissolves. If the opposite is true, the solvent is bad, the chain collpases and the polymer does not dissolve. A solvent, that is a good solvent for one monomer type in a block copolymer and a bad one for the second type of monomer, is called a selective solvent. In case of the block copolymer in the selective solvent, multimolecular micelles or other types of nanostructures can appear. In such a solvent each block has different solubility and solvophobic blocks create micellar cores, while solvophilic blocks form a soluble shell to decrease the number of unfavourable contacts.

Polyelectrolytes (PEs), also called polyions, are polymers made of monomers carrying either positively or negatively charged ionizable group. The charge enormously changes the behaviour of polymers. They usually contain fairly hydrophobic backbone and their solubility is partly due to electrostatic interactions and to the release of small counterions upon dissolution, which increases system entropy [4, 5]. Examples of PEs include synthetic compounds such as polystyrene sulfonate or polyacrylic acid and its salts and many natural polymers such as DNA or proteins.

Experimental study of polymer systems is often very difficult due to their complexity and polydispersity (both in the number of monomer units and the composition) and usually several methods have to be used to get reliable information. Theoretical methods on the other hand use rough approximations, which are sometimes difficult

to verify in mathematical and physical terms. Computer simulations make the interface between them. The adventage is that we can set up exact conditions and study monodisperse polymer, which is very difficult to achieve in experiments. Simulations give detailed and experimentally unreachable results, therefore they make it possible to study different effects independently and thus test theoretical hypotheses. Simulations therefore help both in interpreting experimental data and developing theoretical models.

On the other hand simulations are very demanding both on the computational time and the computer memory, so it is nearly impossible to simulate larger systems at the atomic level. Therefore so-called coarse-grained methods, which group more atoms or molecules into a single particle, are often used.

2. Aim of the thesis

The aim of this work is to contribute the understanding of the electrostatic assembly of diblock copolymers comprised of a water-soluble block and a polyelectrolyte block charged either positively or negatively and the structure of nanoparticles formed. Although a number of experimental studies of polyelectrolyte co-assembly exists, they are focused mainly on development of nano-sized particles for drug delivery. Neither the effect of hydrophobicity of the polyelectrolyte backbone nor the compatibility of the copolymer blocks were studied systematically, because such studies would require a series of samples differing in various parameters, which would be difficult and expansive to prepare.

I study the effect of hydrophobicity of the A-block, incompatibility of the two copolymer blocks, the electrostatics, and compatibility of ions with other components on the aggregation number, structure and compactness of aggregates. The intricate interplay of the above effects is analyzed.

3. Theoretical background

3.1 Polymer self-assembly

Block copolymers in solutions tend to self-assemble and form microphases. In the selective solvent less soluble blocks tend to reduce the number of their unfavourable interactions with solvent by clumping together which drives the creation of a core composed of these blocks and a shell consisting of well soluble blocks. It is therefore an interplay of two forces acting against each other: decreasing enthalpy on one hand and increasing entropy on the other. The structure and symmetry of the copolymer aggregate depends on the relative strengths of the interactions as well as the composition and the architecture of the block copolymers [6]. Block copolymers self-assemble into micelles only above a threshold concentration, so-called critical micelle concentration.

For PEs the electrostatic interactions also affect the self-assembly. In electrostatic assembly the oppositely charged chains (or blocks) tend to associate which comes with a relatively low decrease of entropy that is compensated by the increased entropy of small PE counterions which are released into the bulk solution.

3.2 Counterion condensation

Condensation of counterions plays an important part in PE systems – for example it controls the stability of colloids [7] or self-assembly of biomolecules [8].

The electrostatic attraction between a PE chain and counterions in a solution can result in the condensation of these counterions on the polyion chain [9]. The counterion (Manning) condensation happens due to a fine interplay between the favourable electrostatic attraction of the counterions to the polymer chain and the unfavourable loss of the translational entropy by those counterions due to their localization in the vicinity of the chain [5]. A condensed counterion layer emerges at a critical value of polyion linear charge density and the process of counterion condensation occurs only in the limit of low salt concentration [10].

The linear charge density is measured by the dimensionless Manning parameter $\xi = l_\mathrm{B}/l$, where l is a polymer contour length containing one unit charge [11] and $l_\mathrm{B} = e^2/(4\pi\epsilon_0\epsilon_\mathrm{r}k_\mathrm{B}T)$ is the Bjerrum length – e is electron charge, ϵ_0 is the permittivity of vacuum, ϵ_r is the dielectric constant, k_B is Boltzmann's constant and T represents temperature. The Bjerrum length is defined as the separation at which the electrostatic

interaction between two elementary charges is comparable in magnitude to the thermal motion, $k_{\mathrm{B}}T$ [12]. For a cylinder with a vanishing radius the Manning condensation happens for $\xi > 1$, when the Coulomb interactions dominate over thermal motion. In such case, the number of counterions in the vicinity of the polymer chain increases so that the effective charge density on the polyion reduces to the critical value of $\xi = 1$ [10].

3.3 Computer simulations of polymer solutions

3.3.1 Coarse graining procedures

Even though computer resources are continually increasing, the large number of degrees of freedom and long relaxation times make it impossible to use fully atomistic simulations to study many phenomena including polymer self-assembly. Various coarse-grained models have been applied to tackle such problems and there are many reviews of the used approaches [13, 14, 15].

Using coarse-grained simulations, much larger spatial and time scales can be accessed, which gets us much closer to experiments. Such simulations can also provide a bridge between the atomistic scale and continuum. The ability to link directly the molecular scale to the continuum can minimize errors in the continuum modelling predictions by providing more accurate estimates of the thermodynamic states.

A general strategy of coarse graining is to reduce the number of degrees of freedom through simplification of the model used, retaining only the degrees of freedom important to the phenomena of interest. This comes with a loss of chemical detail, so the trade-off is that the observation of atomistically detailed phenomena is impossible.

Basically, there are two ways to devise a coarse-grained model: bottom-up and top-down approaches. The idea behind the bottom-up approach is to start from the atomistic model and design an effective coarse-grained potential. By grouping several atoms or molecules together, a coarse-grained bead is created, which has lower number of degrees of freedom compared to the initial particles. A possible way to come up with such larger particles for example for polyamide-6,6 is shown in Figure 3.1 [16]. In this model the amide functional group plus one methylene group is replaced by one coarse-grained particle (A), while two particles (B) centered at the second and fifth carbon of the hexamethylene unit, respectively, are used to describe the aliphatic chain. Finally, a third coarse-grained particle (C) is located at the center of mass of the remaining two central methylene units of the tetramethylene unit. Other models with different levels of coarse graining (i.e., different number of physical atoms put together to form a coarse-grained particle) can of course be devised.

Having created these coarse-grained beads, an appropriate potential or force between these beads needs to be found. This is achieved either by structure matching or force matching. The former approach seeks to match features of the structure of the original (i.e., atomistic) system with those of the coarse-grained system that contains less degrees of freedom and find an effective potential reproducing those features. The

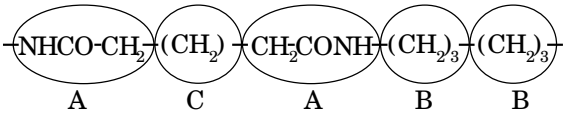

Figure 3.1: Coarse-grained model of polyamide-6,6.

simplest structure feature to use is the radial distribution function (or pair correlation function). This leads to matching of the pair-level structure between the atomistic and the coarse-grained models. To match the structure more completely, higher order correlation functions must be taken into account. In practice, only correlations up to the third order are considered, because determining higher order correlations is not currently feasible [13]. There is a number of methods that can be used to obtain the coarse-grained potential from the known structural features [13].

The second way to obtain the potential is the force matching. As the name suggests, it involves matching forces obtained from the atomistic model with those for the coarse-grained model. This method can determine a pairwise effective forcefield from a given trajectory and force data regardless of their origin, i.e., whether the initial data are obtained from ab initio MD simulations [17] or fully atomistic simulations [18]. During this initial simulation the average force acting on a predefined set of coarse-grained sites (such as the center of mass of a group of atoms) is evaluated. Fitting the resulted data provides parameters for the coarse-grained force [13].

Contrary to the above described bottom-up coarse graining, the top-down approach takes experimental observables (macroscopic properties of the real system such as compressibility, solubility, etc.) to come up with an effective coarse-grained forcefield. Such as in the case of bottom-up coarse graining, some chemical and physical intuition is used. A coarse-grained interaction model with free interaction parameters is assumed and physical observables are fitted to obtain the parameters. A typical example is DPD as derived by Groot and Warren [19], where a soft repulsive force between the coarse-grained beads is assumed and compressibility of water at room temperature along with mutual species solubility is used to obtain the needed parameters. Description of the DPD method is presented in the next section.

3.3.2 Dissipative particle dynamics

DPD is a simulation method similar to molecular dynamics (MD) [19, 20, 21]. MD is a computer simulation technique allowing us to follow the time evolution of a large number of interacting particles. These particles obey the Newton's laws of motion:

$$\mathbf{f}_i = m_i \frac{\mathrm{d}\mathbf{v}_i}{\mathrm{d}t} = m_i \frac{\mathrm{d}^2\mathbf{r}_i}{\mathrm{d}t^2}, \tag{3.1}$$

where $\mathbf{f}_i$ represents a sum of forces acting on a particle i with position vector $\mathbf{r}_i$, velocity vector $\mathbf{v}_i$ and mass m_i; t denotes time. The force is calculated as a negative gradient of an interaction potential. The equations of motion are numerically integrated and thus a new set of particle coordinates and velocities is generated. Macroscopic properties can be then obtained using statistical thermodynamics (see for example [22] for details).

DPD in contrast to MD is an approximate, coarse-grained method by design. This allows us to cover longer time and space scales [23]. In DPD simulations the momentum is conserved, while the total energy is not. DPD fluid is modelled by large beads, each consisting of several molecules or monomers. They interact via force consisting of several pairwise forces:

$$\mathbf{f}_i = \sum_{j \neq i} \left[\mathbf{F}_{ij}^{\mathrm{C}} \left(\mathbf{r}_{ij} \right) + \mathbf{F}_{ij}^{\mathrm{D}} \left(\mathbf{r}_{ij}, \mathbf{v}_{ij} \right) + \mathbf{F}_{ij}^{\mathrm{R}} \left(\mathbf{r}_{ij} \right) \right], \tag{3.2}$$

where the sum goes over all neighbouring particles, which are within a certain cut-off distance, r_c. As this is the only length scale in the system, it is used as a unit of length. Since even in a heterogeneous system, the same value of r_c is used for all beads, it is desirable to have all DPD particles with roughly the same volume [13]. The diameter of these particles is equal to r_c.

As noted before, Groot and Warren [19] assumed all beads interact via a pairwise soft repulsive potential, which is given by equation:

$$u_{ij}^{\mathrm{C}} = \begin{cases} \dfrac{a_{ij}}{2} r_c \left(1 - \dfrac{r_{ij}}{r_c} \right)^2 & \text{for } r_{ij} < r_c \\ 0 & \text{for } r_{ij} \geq r_c \end{cases}, \tag{3.3}$$

where a_{ij} is the maximum repulsion between the particles i and j and r_{ij} is their separation distance. Deriving a negative gradient of the potential gives rise to the conservative force [19, 21]:

$$\mathbf{F}_{ij}^{\mathrm{C}} = -\frac{\mathrm{d}u_{ij}^{\mathrm{C}}}{\mathrm{d}r_{ij}} \mathbf{e}_{ij}, \tag{3.4}$$

where $\mathbf{e}_{ij}$ is a unit vector in a direction of their separation distance [23]. This form makes it possible to use longer simulation timestep [24]. This soft potential allows for significant overlap of DPD particles.

The dissipative force, $\mathbf{F}_{ij}^{\mathrm{D}}$, represents a drag between two particles moving through each other with the relative velocity $\mathbf{v}_{ij}$ [19]:

$$\mathbf{F}_{ij}^{\mathrm{D}} = -\gamma_{ij}\omega^{\mathrm{D}}(r_{ij})(\mathbf{e}_{ij}\cdot\mathbf{v}_{ij})\mathbf{e}_{ij}, \tag{3.5}$$

where ω^{D} denotes a weight function and γ_{ij} is a friction coefficient. The random force, $\mathbf{F}^{\mathrm{R}}$, representing random collisions is given by [19]:

$$\mathbf{F}_{ij}^{\mathrm{R}} = \sigma_{ij}\omega^{\mathrm{R}}(r_{ij})\frac{\zeta_{ij}}{\sqrt{\Delta t}}\mathbf{e}_{ij}, \tag{3.6}$$

where ζ_{ij} is a Gaussian random number with zero mean and unit standard deviation, σ_{ij} a noise amplitude, ω^{R} denotes another weight function and Δt a simulation timestep.

Español and Warren [25] showed that one of the two weight functions in equations (3.5) and (3.6) can be chosen arbitrarily and that this choice fixes the other weight function:

$$\omega^{\mathrm{D}} = \left(\omega^{\mathrm{R}}\right)^2, \tag{3.7}$$

There is also a relation between the coefficents in $\mathbf{F}_{ij}^{\mathrm{D}}$ and $\mathbf{F}_{ij}^{\mathrm{R}}$ [19]:

$$\sigma_{ij}^2 = 2k_{\mathrm{B}}T\gamma_{ij}, \tag{3.8}$$

where k_{B} denotes Boltzmann's constant and T is temperature. These two conditions are derived from the fluctuation-dissipation theorem and the two forces act together as a thermostat.

The repulsive parameter, a_{ij}, is the free interaction parameter in the sense mentioned at the end of the previous section. A macroscopic physical observable must be used to derive the value of this parameter. Groot and Warren [19] utilised compressibility of water at room temperature to derive the following formula:

$$\frac{a_{ii}r_{\mathrm{c}}}{k_{\mathrm{B}}T} = \frac{75}{\rho r_{\mathrm{c}}^3}, \tag{3.9}$$

where $\rho = N/V$ is the particle number density (V being the volume of the system and N the total number of particles). They have also shown that $\rho r_{\mathrm{c}}^3 = 3$ is a good value for the number density [19], therefore $\frac{a_{ii}r_{\mathrm{c}}}{k_{\mathrm{B}}T} = 25$ is the usual choice.

Groot and Warren [19] have also mapped the repulsion parameter for unlike particles onto the Flory-Huggins theory. Comparing the free energy of the DPD and Flory-Huggins models they came up with a simple linear relationship between a_{ij} and the Flory-Huggins parameter, χ_{ij}:

$$\chi_{ij} = 2\alpha_\rho\rho r_c^3\left(a_{ij} - \frac{a_{ii}+a_{jj}}{2}\right)\frac{r_{\mathrm{c}}}{k_{\mathrm{B}}T}, \tag{3.10}$$

where α_ρ is a proportionality constant dependent on ρ. Taking $a_{ii} = a_{jj}$ and $\rho r_c^3 = 3$, it can be shown [19] that:

$$\frac{a_{ij}r_{\mathrm{c}}}{k_{\mathrm{B}}T} = \frac{a_{ii}r_{\mathrm{c}}}{k_{\mathrm{B}}T} + 3.27\chi_{ij} = 25 + 3.27\chi_{ij}, \tag{3.11}$$

since $\frac{a_{ii}r_c}{k_B T} = 25$ is the usual choice. To determine the Flory-Huggins parameter, χ_{ij}, solubility parameters δ_i can be used [26]:

$$\chi_{ij} = \frac{V_{\mathrm{DPD}}}{k_{\mathrm{B}}T} \left(\delta_i - \delta_j\right)^2, \tag{3.12}$$

where V_{DPD} is the volume of a DPD bead.

Polymers in the DPD method are represented by freely jointed chains, which means no restrictions on bond angles is used. Since DPD is a highly coarse-grained method, harmonic spring is sufficient to join the adjacent particles i and $i+1$:

$$\mathbf{F}^{\mathrm{S}}_{i,i+1} = k_{\mathrm{s}} \left(r_{i,i+1} - r_0\right), \tag{3.13}$$

where k_{s} is a spring constant and r_0 is an equilibrium distance between the two beads. This distance is often set to 0, because the repulsive force alone maintains the appropriate distance. The DPD chains are interpenetrating chains (or phantom chains), i.e. the chains pass freely through each other [20].

To integrate the equations of motion the velocity-Verlet algorithm is used:

$$\begin{aligned}
\mathbf{r}_i\left(t+\Delta t\right) &= \mathbf{r}_i(t) + \mathbf{v}_i(t)\Delta t + \frac{1}{2}\left(\Delta t\right)^2 \frac{\mathbf{f}_i(t)}{m_i}, \\
\tilde{\mathbf{v}}_i\left(t+\frac{\Delta t}{2}\right) &= \mathbf{v}_i(t) + \frac{1}{2}\Delta t \frac{\mathbf{f}_i(t)}{m_i}, \\
\mathbf{f}_i\left(t+\Delta t\right) &= \mathbf{f}_i\left[\mathbf{r}_i\left(t+\Delta t\right),\ \tilde{\mathbf{v}}_i\left(t+\frac{\Delta t}{2}\right)\right], \\
\mathbf{v}\left(t+\Delta t\right) &= \mathbf{v}_i(t) + \Delta t \frac{\mathbf{f}_i(t) + \mathbf{f}_i\left(t+\Delta t\right)}{2m_i}.
\end{aligned} \tag{3.14}$$

The velocity prediction, $\tilde{\mathbf{v}}_i$, is needed, because the forces are velocity-dependant. This integrator renders good results and keeps the temperature constant within 1% of the set value for a relatively long timestep of $\Delta t = 0.05$ [27]. Other, more sophisticated integrators developed for DPD simulations are shown in [27].

3.3.3 Electrostatic interactions

Long-range nature of electrostatic forces makes it impossible to simply apply a cut-off radius as is normally done with short-range forces such as $\mathbf{F}^{\mathrm{C}}_{ij}$, $\mathbf{F}^{\mathrm{R}}_{ij}$ and $\mathbf{F}^{\mathrm{D}}_{ij}$. Widely used method to calculate electrostatic forces is the Ewald sum, where overall charge neutrality is necessary. Given N particles, each with a charge q_i and a position vector $\mathbf{r}_i$ in a cubic simulation box of side L and volume $V = L^3$, the total electrostatic energy of the system is

$$U^{\mathrm{el}}\left(\mathbf{r}^N\right) = \frac{1}{4\pi\epsilon_0\epsilon_{\mathrm{r}}} \sum_i \sum_{j \geq i} \sum_{\mathbf{n}} \frac{q_i q_j}{|\mathbf{r}_{ij} + \mathbf{n}L|}, \tag{3.15}$$

where $\mathbf{n}$ is an integer vector, ϵ_0 and ϵ_r are dielectric constants of vacuum and the reference medium, respectively. The sum over $\mathbf{n}$ takes into account the periodic images of the studied system and terms $i = j$ are omitted for $\mathbf{n} = 0$.

In the Ewald sum, the equation (3.15) is decomposed into two parts – a real space sum and a reciprocal space sum [22, 28, 29]:

$$\begin{aligned} U^{\mathrm{el}}\left(\mathbf{r}^N\right) &= \frac{1}{4\pi\epsilon_0\epsilon_r}\left(\sum_i\sum_{j>i} q_i q_j \frac{\mathrm{erfc}(\alpha r_{ij})}{r_{ij}}\right. \\ &+ \left.\frac{2\pi}{V}\sum_{\mathbf{k}\neq 0}^{\infty} Q(k)S(\mathbf{k})S(-\mathbf{k}) - \frac{\alpha}{\sqrt{\pi}}\sum_i^N q_i^2\right), \end{aligned} \tag{3.16}$$

with

$$Q(k) = \frac{1}{k^2}\exp\left(-\frac{k^2}{4\alpha^2}\right), \quad S(k) = \sum_{i=1}^{N} q_i \exp(i\mathbf{k}\cdot\mathbf{r}_i), \quad \mathbf{k} = \frac{2\pi}{L}\mathbf{m}. \tag{3.17}$$

In these equations, $\mathrm{erfc}(x)$ is the complimentary error function; the parameter α controls the contributions from the real and reciprocal space, assuring the convergence of both; k is the magnitude of the reciprocal vector $\mathbf{k}$; $\mathbf{m}$ is an integer vector [22, 28, 29]. Equation (3.16) aproximates $1/r$ given by equation (3.15) very well, capturing its long-range nature.

The electrostatic potential in equation (3.15) diverges at $r = 0$. However the soft DPD potential from equation (3.3) is mathematically well defined there, allowing for a full particle overlap. This leads to a creation of artificial ionic pairs. To overcome this problem, Groot proposed to spread out a point charge into a charged cloud [30]. Groot initially used the linear charge distribution:

$$\rho_{\mathrm{c}}(r) = \begin{cases} \dfrac{3}{\pi r_{\mathrm{e}}^3}\left(1 - \dfrac{r}{r_{\mathrm{e}}}\right) & \text{for } r < r_{\mathrm{e}} \\ 0 & \text{for } r \geq r_{\mathrm{e}} \end{cases}, \tag{3.18}$$

where r_{e} is the electrostatic smearing radius. The electrostatic field is then solved on a lattice according to work of Beckers [32]. Other charge distributions were suggested. Recently Warren et al. proposed a normalised Gaussean smearing [33]:

$$\rho_{\mathrm{c}}(r) = \left(2\pi\sigma^2\right)^{-\frac{3}{2}}\exp\left(-\frac{r^2}{2\sigma^2}\right), \tag{3.19}$$

where σ is a size of the Gaussian charge cloud.

The charge density distribution implemented in the DL_MESO simulation package that I use for my simulations has a Slater-type charge distribution [28]:

$$\rho_{\mathrm{c}}(r) = \frac{1}{\pi\lambda_{\mathrm{e}}^3}\exp\left(-\frac{2r}{\lambda_{\mathrm{e}}}\right), \tag{3.20}$$

where λ_e is the Slater decay length of the charge distribution. It is impossible to calculate potentials and forces using this Slater-type charge density analytically, but there are good aproximations [34]. The interaction potential between two charged distributions separated by a distance r_{ij} is [28]:

$$U_{ij}^{\mathrm{el}} = \frac{l_B q_i q_j}{r_{ij}} \left[1 - (1 + \beta r_{ij}) \exp\left(-2\beta r_{ij}\right)\right], \tag{3.21}$$

where $\beta = 5/(8\lambda_e)$. The Bjerrum length of $l_B = 1.1$ (in reduced units) then represents aqueous solution.

The reduced force between two charge distributions is [28]:

$$F_{ij}^{\mathrm{el}} = \frac{l_B q_i q_j}{r_{ij}^2} \left\{1 - \exp\left(-2\beta r_{ij}\right)\left[1 + 2\beta r_{ij}(1 + \beta r_{ij})\right]\right\}. \tag{3.22}$$

Using equations (3.21) and (3.22) the divergency of the classical Coulombic term at $r_{ij} = 0$ is removed and the energy between two charged distributions at $r_{ij} = 0$ is a finite quantity:

$$\lim_{r_{ij} \to 0} U_{ij}^{\mathrm{el}} = q_i q_j \beta l_B. \tag{3.23}$$

Therefore the force at $r_{ij} = 0$ is $\lim_{r_{ij} \to 0} F_{ij}^{\mathrm{el}} = 0$.

Since the DPD method requires all beads to have roughly the same volume, a charged polymer bead representing a Kuhn segment is of the same size as its small counterion. In reality the counterion is much smaller and therefore in DPD this ion is thought of as a solvated ion.

3.3.4 Reduced units and parameter mapping

Since it is impractical to use classical SI units in computer simulations, because they are either too small or very large, a set of reduced units is employed [22]. The unit of length is the cut-off distance of the repulsive DPD forces acting on the particles r_c. The energy is measured in units of $k_B T$. The third one is the unit of mass of the particle m_i.

Where the reduced units are used, the noise amplitude σ_{ij} and the particle density ρ are both equal to 3 in accordance with Groot and Warren [19]. The friction coefficient in the dissipative force $\gamma_{ij} = \sigma_{ij}^2/2 = 4.5$. The dimensionless timestep Δt has been chosen as 0.05 in all the simulations performed in this work.

The relations between these reduced units and the real units is (in contrast to the rest of the text, an asterisk denotes reduced units):

$$a_{ij}^* = \frac{a_{ij} r_c}{k_B T}, \quad \rho^* = \frac{N r_c^3}{V} = \frac{r_c^3}{V_{\mathrm{DPD}}}, \tag{3.24}$$

The time unit was calculated by Groot and Rabone [35] on the basis of self-diffusion of water as:

$$t = (14.1 \pm 0.1) N_m^{5/3} \ \ [\mathrm{ps}], \tag{3.25}$$

where N_m is the number of physical water molecules in one DPD bead. One simulation timestep therefore corresponds to $(t \cdot \Delta t)$ ps in real time.

To map a real polymer system onto the DPD model, several methods can be used to determine the number of beads representing a specific polymer, n_DPD [36]. For example, the characteristic ratio of the polymer, C_n, representing in simple terms the number of monomers in one Kuhn segment, can be used [37]:

$$n_\mathrm{DPD} = \frac{M_\mathrm{n}}{M_\mathrm{m} C_\mathrm{n}}, \tag{3.26}$$

where M_n and M_m are the molar masses of the polymer and monomer, respectively. There are empirical methods to determine C_n [37], which is typically between 7 and 10.

Knowing the value of C_n, the volume of DPD particle can be determined as $V_\mathrm{DPD} = C_\mathrm{n} V_\mathrm{m}$, where V_m is the volume of one monomer. From there, the number of water molecules in one solvent bead and other real units can be easily calculated using the relations in equations (3.24) and (3.25).

4. Simulation details

All simulations were performed using the simulation software DL_MESO [38]. This simulation package has been developed at Daresbury Laboratory for the United Kingdom Collaborative Computational Project known as CCP5. It is a parallel mesoscale simulation package capable of dissipative particle dynamics and the lattice Boltzmann equation method. For data processing I have created my own software package.

4.1 Electrostatic smearing

The decay length of the charge distribution, λ_e, was chosen by González-Melchor [28] to be 0.67 in accordance with the magnitude of Groot's electrostatic force at $r = 0$ [30]. However, this means a significant part of the charge is localised outside a bead. I have chosen a smearing constant $\lambda_e = 0.2$, which confines almost all the charge inside the bead as shown in our recent paper [31]. Figure 4.1 depicts the distribution of the charge in the charged cloud for both values of λ_e and it clearly shows the charge is spread out up to the reduced distance $r \approx 3$ for $\lambda_e = 0.67$, while for $\lambda_e = 0.2$ the charge remains confined to the DPD bead (diameter of a DPD bead is $r = 1$ as explained

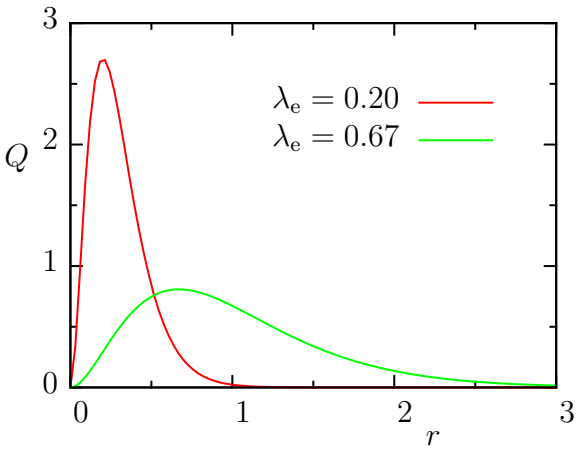

Figure 4.1: Distribution of charge, $Q(r)$, inside a charged cloud with exponential charge density for both values of Slater decay length, λ_e.

above).

The definition of the Bjerrum length as stated in Section 3.2 requires the electrostatic interaction at distance of $r = l_B$ to be $-k_BT$. Figure 4.2 clearly shows the value of $\lambda_e = 0.2$ is the largest Slater decay length satisfying the condition in aqueous environment (i.e., for $l_B = 1.1$), while the potential for the value of $\lambda_e = 0.67$ is significantly higher.

A comparison of electrostatic potential, Equation (3.21), and force, Equation (3.22),

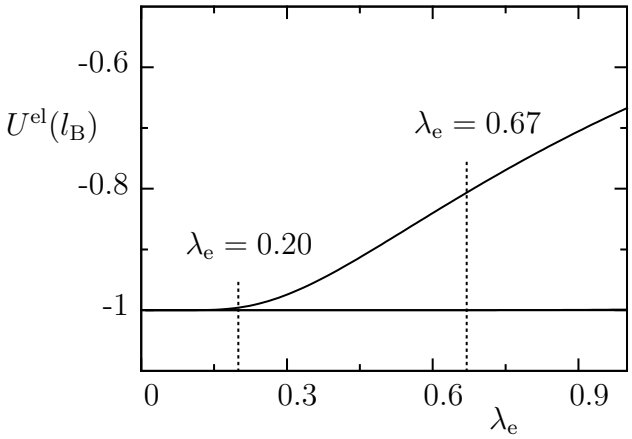

Figure 4.2: The dependence of the electrostatic potential between two smeared elementary charges of opposite sign for a separation distance $r = l_B = 1.1$ (aqueous conditions) as a function of the charge decay length, λ_e.

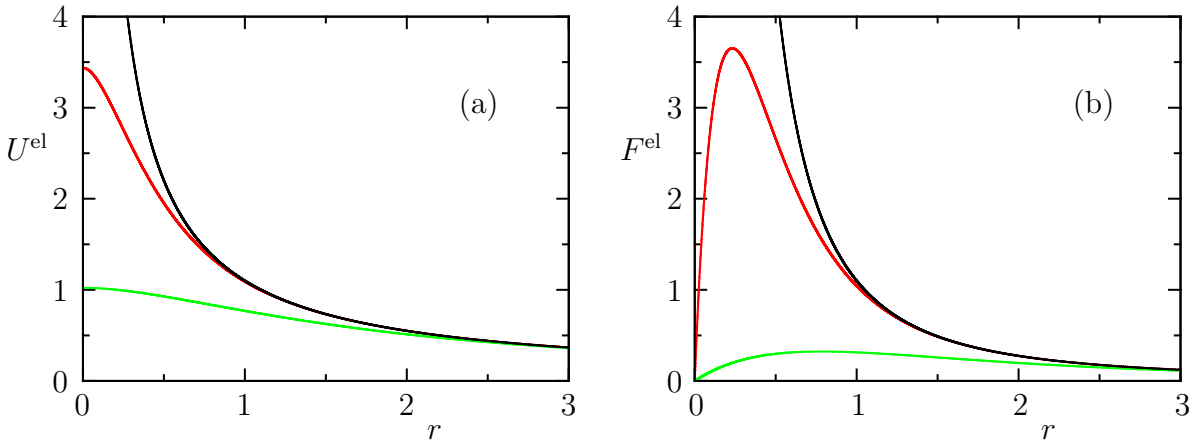

Figure 4.3: (a) Electrostatic potential, U^{el}, between two charged clouds with charges +1 for the two values of λ_e and Coulombic potential in aqueous conditions ($l_B = 1.1$). (b) Electrostatic force, F^{el}, between the same charged clouds, again for the two values of λ_e and Coulombic force. Red and green lines represent the cases of $\lambda_e = 0.2$ and 0.67, respectively, while the black lines shows Coulombic potential (or force).

for these two values of λ_e are shown in Figures 4.3a and 4.3b, respectively. Also a Coulombic potential and force is added. The localisation of the whole charge within the bead yields much steeper potential (and force) in the region of smaller distances. Therefore it is more similar to the Coulombic potential (and force) and the electrostatics plays more important role at short distances. Results for differently smeared systems should differ for inter-particle distances of up to $r = 3$, since neither charged cloud

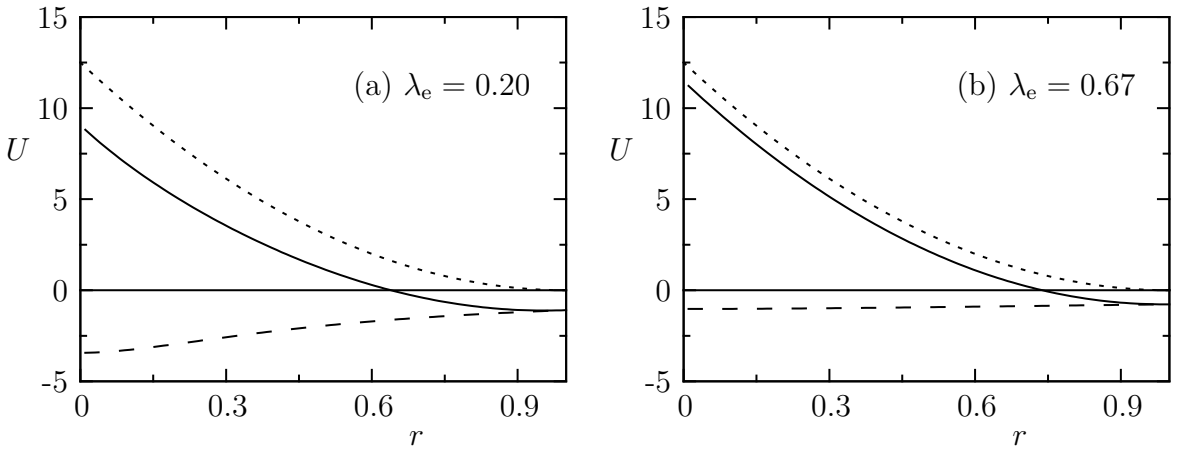

Figure 4.4: Sum of the DPD repulsive potential with $a_{ij} = 25$ and the smeared electrostatic potential of two oppositely charged clouds (with charges +1 and −1) for: (a) $\lambda_e = 0.2$ and (b) $\lambda_e = 0.67$. Full lines represent the sum of electrostatic and repulsive potential, which are drawn in dashed and dotted lines, respectively.

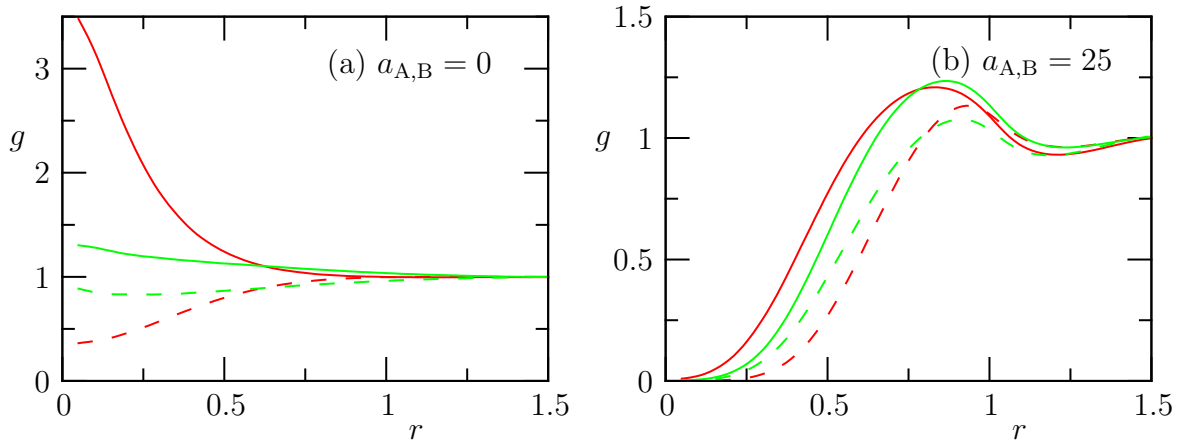

Figure 4.5: Radial distribution function, g, for the mixture of opositely charged beads for both types of charge smearing for: (a) $a_{A,B} = 0$ and (b) $a_{A,B} = 25$. Red lines correspond to $\lambda_e = 0.2$, while the green lines represent $\lambda_e = 0.67$. Full lines are radial distribution functions between unlike particles, $g_{A\text{-}B}$, and the dashed ones are radial distribution functions between like particles, $g_{A\text{-}A}$ and $g_{B\text{-}B}$.

extends beyond that and therefore the potential is the same for $r > 3$.

To further investigate the difference between the two potentials with different λ_e I have performed simulations of a mixture of oppositely charged particles A and B (i.e., salt melt), where $q_A = 1$ and $q_B = -1$, without DPD repulsion ($a_{A,B} = 0$). This is unphysical system, because the only interaction between the particles is the electrostatic force (along with thermal motion represented by dissipative and random forces), but it can be of some use. The radial distribution functions, g, are shown in Figure 4.5a for both values of λ_e. There we see the thermal motion itself is enough to cancel out the effect of opposite charges almost completely in the case of $\lambda_e = 0.67$. On other hand the lower value of λ_e ensures every bead is surrounded by beads of opposite charge, which is the result expected with the repulsive force turned off. Switching on the inter-particle repulsion by setting $a_{A,B} = 25$ significantly decreases the difference as seen in Figure 4.5b.

I have carried out simulations for both values of λ_e and the comparison is presented in Chapter 5.

4.2 Studied systems

Two different polymer systems were investigated in this thesis and the results are presented and discussed in Chapter 5. Here only a short description is provided and a more detailed one is shown in Section 4.4.

Firstly the counterion condensation was reproduced to show that DPD is suitable to study PEs. The system comprised of a single linear polymer chain formed by 50 beads, A_{50}, and 50 counterions (CI) in a box of solvent (S). The chain was solvophobic which was represented by a high repulsion parameter $a_{A,S}$. The polymer and counterion beads had a unit charge of opposite magnitude. The volume of the simulation box was 30^3, so the total number of DPD beads was 81000. In this system the value of Bjerrum length, l_B, was varied. A neutral system was simulated for comparison.

The main purpose of this thesis is the study of PE self-assembly. The second system therefore comprised of copolymer chains, A_5B_5, with one water-soluble neutral block and one block charged either positively (A^+ beads) or negatively (A^- beads) and counterions (CI or I^+ and I^-) in a box of solvent. All charged beads had a unit charge. The volume of the simulation box was 25^3 with the total number of particles 46875. This smaller box was chosen, because of the high number of simulations performed and because long simulation runs had to be done to achieve good statistical results. There was 5.1 vol% of polymer in the simulation box, which represents 240 copolymer chains (half with positively charged A-block and half with negatively charged one). The number of counterions varied to represent a system with and without added salt. Also the solvophobicity of the A-block and the compatibility of the two blocks were varied to study their effect on the self-assembly. Again, neutral systems were simulated to show the effect of electrostatic assembly.

4.3 Data analysis

4.3.1 Aggregation number

Aggregation (or association) number, A_s, is the number of chains in one aggregate. Weight-average aggregation number is defined as

$$\langle A_\mathrm{s} \rangle_\mathrm{w} = \frac{\sum_i m_i^2}{\sum_i m_i}, \tag{4.1}$$

where m_i is the weight of an aggregate i.

Weight distribution function of aggregation numbers, F_w, is defined as:

$$F_\mathrm{w}(A_\mathrm{s}) = \frac{m_{A_\mathrm{s}} N_{A_\mathrm{s}}}{\sum_i m_i N_i}, \tag{4.2}$$

where m_i is the mass of an aggregate with association number $A_\mathrm{s} = i$ and N_i is the number of such aggegates. Similarly defined is the number distribution of aggregation numbers, F_n:

$$F_\mathrm{n}(A_\mathrm{s}) = \frac{N_{A_\mathrm{s}}}{\sum_i N_i}. \tag{4.3}$$

Both these functions are normalised, therefore the value of F_w (or F_n) provides information of what fraction of aggregates with given mass (or aggregate number) is in the system.

To obtain information about self-assembly of copolymers, aggregates have to be defined first. In this work a simple criterium is used to discern aggregates from free

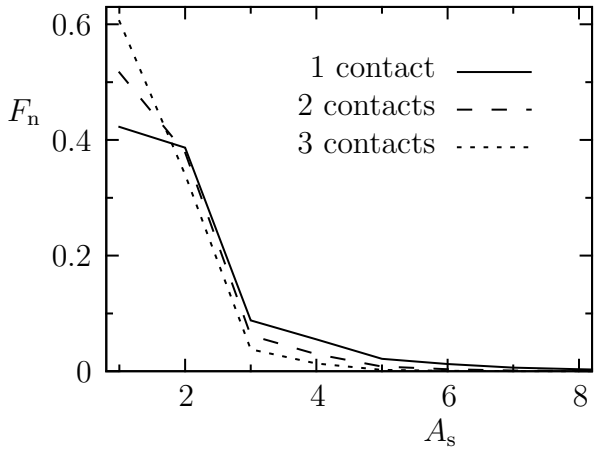

Figure 4.6: Comparison of three possible aggregation criteria shown on the number distribution function, F_n, of the charged copolymer system with $a_{\mathrm{A,S}} = a_{\mathrm{B,S}} = a_{\mathrm{A,B}} = 25$.

chains. Number of contacts between every two chains is calculated, where the contact is registered if two solvophobic beads from different chains have separation lower then 1 (in reduced units). Then, if the number of contacts of these two chains is higher or equal than a predetermined value, these chains are in one aggregate.

Comparison of three such criteria (1, 2 and 3 contacts needed for two chains to form an aggregate) is in Figure 4.6. The number distribution function, $F_{\mathrm{n}}(A_{\mathrm{s}})$, for a charged system of double-hydrophilic copolymers, $\mathrm{A_5B_5}$, with compatible blocks ($a_{\mathrm{A,S}} = a_{\mathrm{A,B}} = a_{\mathrm{B,S}} = 25$) is plotted there. The system is described in detail in Section 4.4. The differences between the three criteria in this case are significant for unimers, but much smaller for higher aggregation numbers, A_{s}. Other simulated systems with higher values of repulsion parameters between A beads and solvent, $a_{\mathrm{A,S}}$, show even smaller differences. All results in Section 5.2 were obtained via the criterium of 2 contacts.

4.3.2 Gyration tensor

The radius of gyration is defined as the root mean square of the average squared distance of beads in a chain or aggregate from its center of gravity, $\mathbf{r}_{\mathrm{CM}}$ (assuming all particles have the same mass):

$$R_{\mathrm{g}}^2 = \frac{1}{N}\sum_{i=1}^{N}(\mathbf{r}_i - \mathbf{r}_{\mathrm{CM}})^2, \tag{4.4}$$

where N is the number of particles forming the chain or aggregate.

In this work, the radius of gyration is calculated using a gyration tensor, $\mathbf{S}$, which describes the second moments of the position vectors of the beads:

$$S_{mn} = \frac{1}{N}\sum_{i=1}^{N}(r_i^m - r_{\mathrm{CM}}^m)(r_i^n - r_{\mathrm{CM}}^n), \tag{4.5}$$

where r_i^m stands for the m-th Cartesian coordinate of $\mathbf{r}_i$ and r_{CM}^m is the m-th Cartesian coordinate of $\mathbf{r}_{\mathrm{CM}}$. The gyration tensor is a symmetric matrix which can be diagonalised:

$$\mathbf{S} = \begin{pmatrix} \lambda_x^2 & 0 & 0 \\ 0 & \lambda_y^2 & 0 \\ 0 & 0 & \lambda_z^2 \end{pmatrix}, \tag{4.6}$$

where λ_x^2, λ_y^2 and λ_z^2 are eigenvalues chosen so that $\lambda_x^2 < \lambda_y^2 < \lambda_z^2$ [39].

These eigenvalues may be used to determine several properties. The radius of gyration is calculated as:

$$R_{\mathrm{g}}^2 = \lambda_x^2 + \lambda_y^2 + \lambda_z^2. \tag{4.7}$$

The shape descriptors, asphericity b and acylindricity c, are defined as [40]:

$$b = \lambda_z^2 - \frac{1}{2}(\lambda_x^2 + \lambda_y^2), \quad c = \lambda_y^2 - \lambda_x^2. \tag{4.8}$$

The asphericity is always a non-negative value equalling zero only when the particles are distributed with spherical symmetry (or symmetry with respect to all three coordinate axes). The acylindricity is also non-negative and attains zero only when the distribution of particles is cylindrically symmetric (or symmetric with respect to the two axes).

Using all three descriptors, R_g, b and c, the relative shape anisotropy, κ^2 can be obtained as: [40]:

$$\kappa^2 = \frac{b^2 + 0.75c^2}{R_g^4}. \tag{4.9}$$

The relative shape anisotropy is bound between zero and one. For a structure of tetrahedral or higher symmetry (for example a spherical aggregate, $\lambda_x = \lambda_y = \lambda_y$), the relative shape anisotropy goes to 0. The value $\kappa^2 = 0.25$ corresponds to a regular planar structure ($\lambda_x = 0$ and $\lambda_y = \lambda_z$). Prolate cylindrical structures are characterised by $\kappa^2 = 1$ ($\lambda_x = \lambda_y = 0$) [41].

4.3.3 Autocorrelation function

The coordinates and velocities generated during the simulations are correlated, because only a small change happens between two successive steps. Therefore the relaxation time, τ, which represents the number of steps between two uncorrelated states, have to be estimated for each physical property [42]. The ACF as a function of a time-lag i for a quantity X is calculated as:

$$\mathrm{ACF}(i) = \frac{\langle X_{j+i} X_j \rangle - \langle X \rangle^2}{\sigma^2}, \tag{4.10}$$

where $\langle X \rangle$ is the mean of the quantity X, $\langle X^2 \rangle$ is its mean square, $\langle X_{j+i} X_j \rangle = \frac{1}{n-i} \sum_{j<n-i} X_{j+i} X_j$ (n is the total number of "times") and $\sigma^2 = \langle X^2 \rangle - \langle X \rangle^2$ is the variance.

It can be shown that the ACF asymptotically decreases as an exponential function [42]. Thus to acquire an approximate τ, we may fit the ACF by the exponential curve in the form $a \exp\left(-\frac{x}{\tau}\right)$; the constant a, which should approach 1, is added so that the exponential curve gives a better fit. Using τ twice as large suffices and a deeper look into the autocorrelation is unnecessary.

To determine how often to save the configurations during a simulation, a short simulation run is done first with very frequent data gathering and autocorrelation function is determined for some physical quantity. An example of an autocorrelation function is shown in Figure 4.7, where the weight-average aggregation number for a neutral copolymer system with mildly solvophobic A-block ($a_{A,S} = a_{A,B} = 32.5$ and $a_{B,S} = 25$) is used. Also an exponential fit can be seen there and the relaxation time is $\tau = 9.8$. In this short simulation, the configurations were saved every 50 timesteps. The longer simulation is then performed and in this case every 1000-th configuration is saved for analysis.

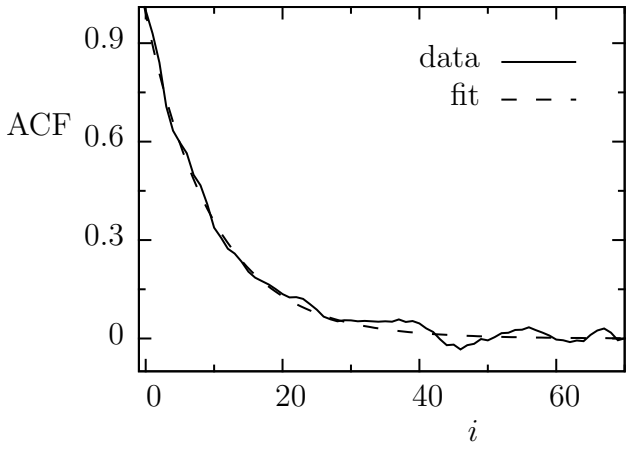

Figure 4.7: Autocorrelation function of the weight-average aggregation number for the neutral system in mildly solvophobic A-block. Fit: $\mathrm{ACF}(i) = 0.99\exp(-i/9.8)$.

4.4 Parameters of studied systems

In all the simulations, the repulsive coefficients between the same species, a_{ii}, were set to 25 and the simulation timestep was $\Delta t = 0.05$. The noise amplitude, σ_{ij}, was 3 and therefore the friction coefficient $\gamma_{ij} = 4.5$. The particle density was $\rho = 3$ as is typical in DPD. The mass of all beads was set to 1. For the harmonic spring potential, the parameters were $k_\mathrm{s} = 4$ and $r_0 = 0$.

The electrostatic forces were treated using the Ewald sum with the cut-off distance of 3, real-space convergence paramater $\alpha = 0.975$ and reciprocal vector range $\mathbf{n} = (5,5,5)$.

As described above, the first studied system consisted of a single solvophobic polymer chain comprised of 50 beads, A_{50}, 50 counterions and solvent particles. The charges were $q_\mathrm{A} = 1$ and $q_\mathrm{CI} = -1$ in units of elementary charge. The value of the Bjerrum length was varied between 0.1 and 7. Two sets of simulations with two values of charge smearing, $\lambda_\mathrm{e} = 0.2$ and 0.67, were performed. The repulsive parameters, a_{ij}, and the corresponding Flory-Huggins parameters, χ_{ij} are shown in Table 4.1. Also a

a_{ij}	A	CI	S
A	25	40	40
CI		25	25
S			25

χ_{ij}	A	CI	S
A	0	4.5	4.5
CI		0	0
S			0

Table 4.1: Repulsion coefficients, a_{ij}, and the corresponding Flory-Huggins parameters, χ_{ij}, between all bead types for simulations of counterion condensation.

corresponding neutral system was simulated for comparison.

Figure 4.8 shows the sum of the repulsive and the electrostatic potential for three values of the Bjerrum length, l_B, for both values of λ_e. For $l_B = 7$ and $\lambda_e = 0.2$, the potential is negative from the beginning. Since DPD beads are soft particles, this does not necessarily present a problem. However, the potential at $r = 0$ cannot be too negative, because otherwise the thermal motion would not be strong enough to separate the two beads and artificial ionic pairs might appear. Therefore $l_B = 7$ is the largest value used in this work, when the potential at $r = 0$ is approximately -1, which is about the same magnitude as the thermal motion ($k_BT = 1$). For higher values of the Bjerrum length, the system is unphysical.

All simulations started from random configuration. In all the simulations, after equillibrating for 10^5 timesteps I ran 10^6 timesteps, collecting data every 10^3 timestep. This gave me 10^3 independent configurations for analysis. The results and discussion of the counterion condensation are presented in Section 5.1.

The main purpose of this work is to investigate the self-assembly of diblock copolymers, A_5B_5, containing one neutral water-soluble block (B-block) and one block with varying solubility charged either positively or negatively (A_5^+ or A_5^--block). I have studied a system consisting of A_5B_5 chains in a mixture of solvent (S) and counterion (CI or I^+ and I^-) particles. All charged beads had a unit charge. As mentioned above, the volume fraction of polymer beads was 5.1 vol%, which corresponds to 240 copolymer chains in the simulation box with the size 25^3. Half of those were positively charged and half negatively. To investigate the effect of electrostatic assembly, corresponding neutral systems were simulated for comparison.

B-block was solvophilic with $a_{B,S} = 25$ (corresponding to the Flory-Huggins parameter $\chi_{B,S} = 0$). The solubility of the A-block, $a_{A,S}$, was varied from 25 to 37.5 (from

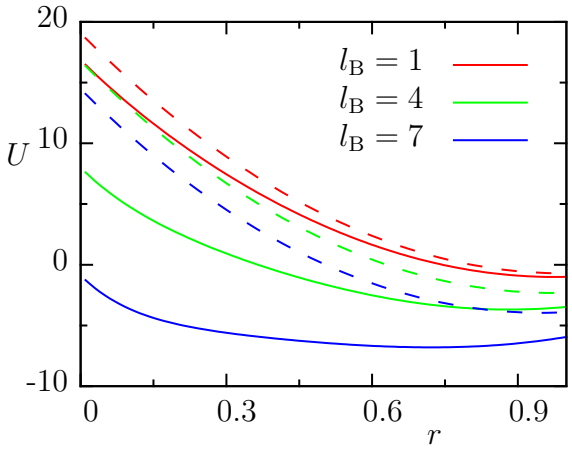

Figure 4.8: Sum of DPD repulsive potential (with $a_{ij} = 40$) and electrostatic potential for different values of l_B for both values of λ_e. Lines of one colour represent potentials with the same l_B, where a full line shows the potential with $\lambda_e = 0.2$ and a dashed line the one with $\lambda_e = 0.67$.

		$a_{A,B}$				
		25.0	30.0	32.5	35.0	37.5
$a_{A,S}$	25.0	×[a]		×		×[a]
	32.5	×	×	×		×
	35.0	×[a]	×[a]		×[a,b]	×
	37.5	×	×		×	×[a]

Table 4.2: Studied systems with different values of repulsion parameters $a_{A,S}$ and $a_{A,B}$. With the marked systems, three simulations were always performed: neutral system, charged system without salt and charged system with 5 vol.% of salt; both for $\lambda_e = 0.2$.
[a] also simulated charged systems with $\lambda_e = 0.67$.
[b] also simulated charged systems with $a_{CI,A} = 25$ for $\lambda_e = 0.2$.

well soluble $\chi_{A,S} = 0$ to solvophobic $\chi_{A,S} = 3.8$). Also the compatibility of the two blocks, $a_{A,B}$, was varied between 25 and 37.5. Typically, the values of a_{ij} for counterions were the same as those for solvent beads, but in some cases the counterions were compatible with the solvophobic A beads ($a_{A,CI} = 25$).

I have performed simulations with the number of counterions corresponding to the number of A beads and simulations with 5 vol% of salt added. Simulations with both values of charge smearing, $\lambda_e = 0.2$ and 0.67, were performed for some systems to further compare the different electrostatic potentials. All simulated systems are clearly shown in Table 4.2, where the symbol × represents the three simulations done for the given pair of repulsion coefficients – neutral system and charged systems both with and without salt for $\lambda_e = 0.2$.

Most simulations started from random configuration, but a few were initiated from aggregated state to prove ergodicity of the simulations. The equilibration period was 10^6 timesteps and another $(2-5) \cdot 10^7$ timesteps were performed to collect data. The results and discussion are presented in Section 5.2.

5. Results and discussion

5.1 Counterion condensation

The simulation of counterion (or Manning) condensation was performed to show that the electrostatics in the DPD method work correctly. The strength of the electrostatic interactions in these simulations was controlled by the Bjerrum length.

Snapshots of typical conformations of the neutral and charged PE chain are shown in Figure 5.1 and Figure 5.2, respectively. It can be seen that even a small value of l_B is enough to prevent the PE chain from collapsing due to its hydrophobicity. With increasing value of l_B the chain begins to collapse again due to the counterion condensation which compensates the charges and therefore the hydrophobic nature of the PE backbone prevails again. This is more pronounced for lesser charge smearing, i.e. for simulations with $\lambda_e = 0.2$ (upper row of snapshots in Figure 5.2).

Figure 5.3 shows the fraction of counterions that are closer to the chain then $r = 1$ (full lines) and $r = 3$ (dashed lines) for different values of l_B. The limit value of distance r was set to three, because up to this distance the electrostatic potentials with different charge smearing differ. The second limit value of distance r was set to the cut-off distance of the DPD forces, because at this distance the polymer bead and the counterion are in contact and therefore the counterion may be regarded as truly condensed. The fraction of the condensed counterions increases with increasing value of the Bjerrum length (i.e. with the strengthening of the electrostatic force) as expected, but the increase is larger for $\lambda_e = 0.2$ in the case of contact distance $r = 1$. For the systems with the highest value of l_B, about 90% of the counterions are located on the PE chain, while for $\lambda_e = 0.67$ only about 60% of the counterions are condensed. As expected, the results for the limit value of distance $r = 3$ are the same for both charge

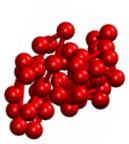

Figure 5.1: Snapshot of a typical conformation of the neutral polymer chain.

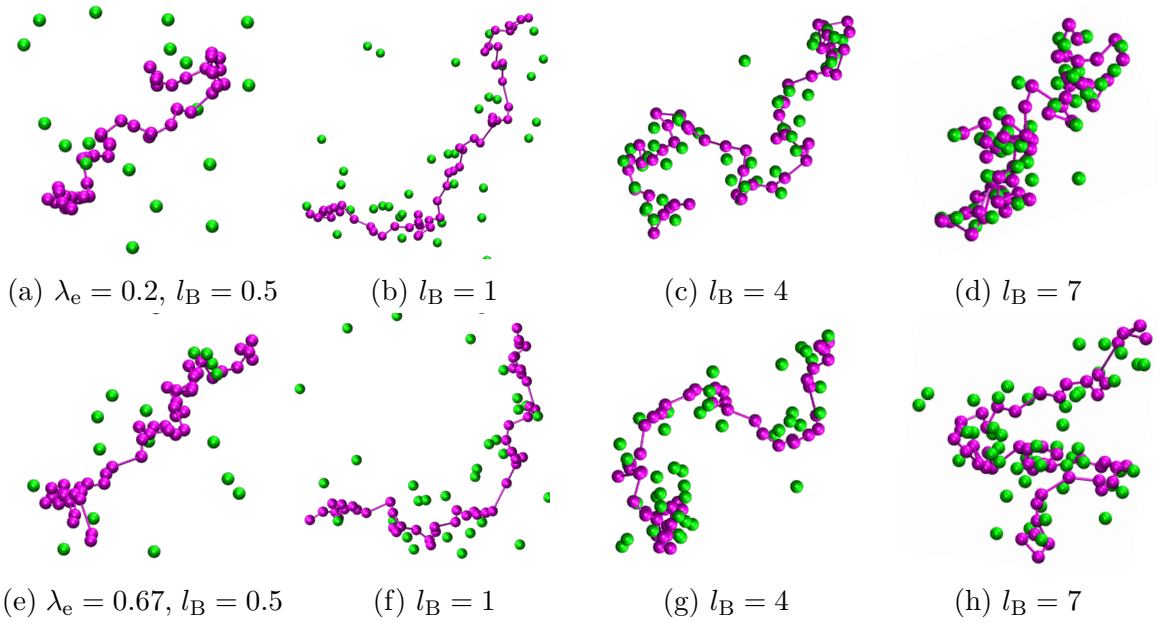

(a) $\lambda_e = 0.2$, $l_B = 0.5$ (b) $l_B = 1$ (c) $l_B = 4$ (d) $l_B = 7$

(e) $\lambda_e = 0.67$, $l_B = 0.5$ (f) $l_B = 1$ (g) $l_B = 4$ (h) $l_B = 7$

Figure 5.2: Snapshots of typical conformations of the PE chain with the two values of λ_e and different values of the Bjerrum length, l_B. Violet beads represent the PE chain and green ones the counterions.

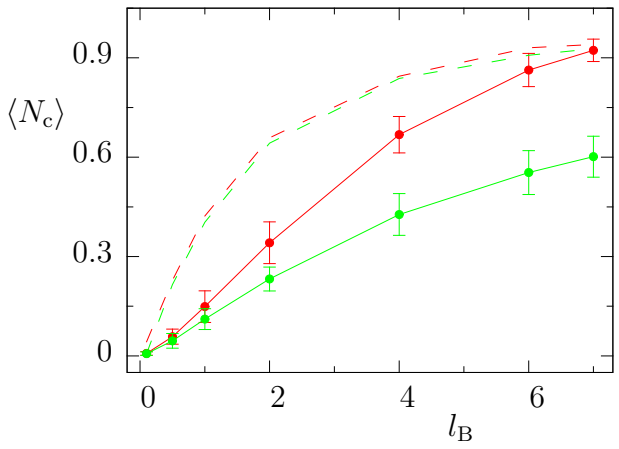

Figure 5.3: Average fraction of condensed counterions, $\langle N_c \rangle$, as a function of the Bjerrum length, l_B. Red lines represent systems with $\lambda_e = 0.2$ and green ones show results for $\lambda_e = 0.67$. Full lines show fraction of counterion in the distance $r \leq 1$ from the PE chain, while the dashed lines represent their fraction in the distance $r \leq 3$ from PE chain.

decay lengths as their electrostatic potentials differ at distances $r \leq 3$.

Using the results from Figure 5.3 an effective charge on the PE chain can be calculated as the net charge on the PE chain reduced by the charge of the condensed counterions and therefore the value of the Manning parameter, ξ, can be determined. Calculating the Manning parameter in the simulations with the highest value of the Bjerrum length ($l_B = 7$) for the systems with different charge smearing shows the system with $\lambda_e = 0.2$ is closer to the expected value of $\xi = 1$ with $\xi \approx 0.8$, while for the system with $\lambda_e = 0.67$ the Manning parameter is $\xi \approx 3$.

In Figure 5.4 the radius of gyration, R_g, and the relative shape anisotropy, κ^2, are plotted against the Bjerrum length, l_B. These graphs show the neutral (or undissociated) chain is totally collapsed with the smallest value of R_g and spherical symmetry (κ^2 is near 0). With the increase of the Bjerrum length, both R_g and κ^2 increase, i.e. the PE chain expands. The value of κ^2 indicates it is relatively close to cylindrical symmetry. The PE chain is expected to be most expanded (or to have the largest value of R_g) for the Manning parameter $\xi = 1$. The average separation distance between neighbouring beads in the chain for lower values l_B is $l \approx 0.8$, so the value of Bjerrum length should be $l_B = \xi l = 0.8$. Presence of the peak at $l_B = 1$ therefore fulfills the expectations. For higher values of the Bjerrum length, the counterion condensation starts affecting the PE chain. The condensed counterions reduce the effective charge of the PE chain to keep the Manning parameter near the value of one. Due to this compensation of the charges the hydrophobic nature of the PE backbone starts to prevail and the PE chain collapses.

The difference between the two types of charged clouds is clearly visible. For the lower values of l_B the systems with different charge smearing behave similarly, although the chain in the systems with $\lambda_e = 0.2$ is slightly more expanded due to the steeper elec-

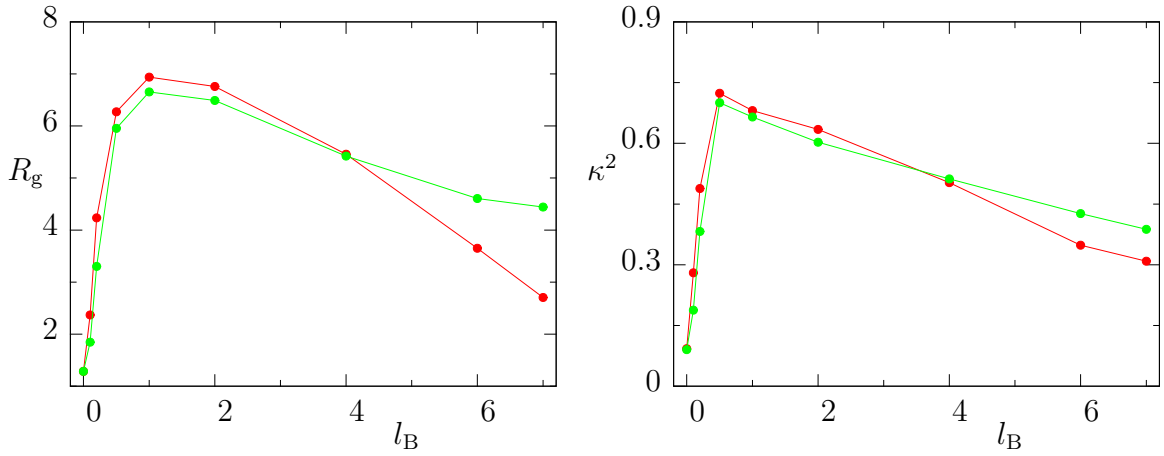

Figure 5.4: Radius of gyration, R_g, and relative shape anisotropy, κ^2, as functions of the Bjerrum length, l_B. Red lines represent systems with $\lambda_e = 0.2$ and green lines systems with $\lambda_e = 0.67$

trostatic potential. For larger values of l_B this steeper electrostatic potential attracts more counterions to the PE chain, forcing it to collapse more due to the hydrophobicity of its backbone than in the case of systems with $\lambda_e = 0.67$.

These results show both that DPD has well implemented electrostatic interactions and that the lower value of $\lambda_e = 0.2$ is a good choice to smear a point charge into a cloud.

5.2 Self-assembly of copolymer chains

In this section, the main results of my work are presented. As explained above, the electrostatic forces alone do not control the aggregate size or architecture. They affect the polymer self-assembly, but the effect of hydrophobicity of the charged block and the compatibility of the two blocks also play an important role.

The increase of the hydrophobicity of the A-block is expected to promote the creation of larger aggregates. Copolymers with incompatible A and B-blocks are expected to form well pronounced core-shell structures, while in the systems with the compatible A and B-blocks the aggregate core is expected to include both A and B-blocks.

Figure 5.5 shows the weight and number distribution functions for the double-hydrophilic system ($a_{A,S} = 25$) for all three possibilities (neutral system, 50%-to-50% mixture of $A_5^+B_5$ and $A_5^-B_5$ copolymers with the corresponding number of counterions and the analogous charged system with 5 vol% of added salt). As both blocks are soluble, the neutral copolymer is fully dissolved. The non-negligible number of small aggregates with A_s equal to 2 and 3 is a result of random collisions.

The presence of opposite charges on different chains leads to the electrostatic self-assembly. With the well soluble charged A-block, no large aggregates are expected to form, because after the compensation of the charges the resulting dimer is soluble. As the charges at the PE chains are mutually interconnected, the cooperative character of electrostatics promotes the self-assembly. The change of electrostatic potential energy is very small, because it depends on the charges and its distances, not on the type of charge carrier. Since the diblock is well soluble, there is no advantage in the formation of domains rich in A beads and the enthalpic term in this case is negligible. Therefore the self-assembly is entropy controlled. The association of several copolymers is accompanied by a translational entropy increase of liberated mobile counterions and a small entropy decrease of the diblocks. In the case of charged systems without salt (Figures 5.5b and 5.5e for the weight and number distributions, respectively) a very large population of dimers is seen for $\lambda_e = 0.2$, which is in accordance with experimental knowledge. On the other hand, with the value of charge smearing $\lambda_e = 0.67$, the number of dimers is far lower and the distributions are close to those of the neutral system. For this value of smearing, the electrostatic cloud has a radius three times grater than the bead size (see Figure 4.1), so such parameterization is not proper for the description of electrostatic interactions of small ions. Adding salt to the system dissolves the dimers just as expected. The effect of diblock incompatibilty is negligible

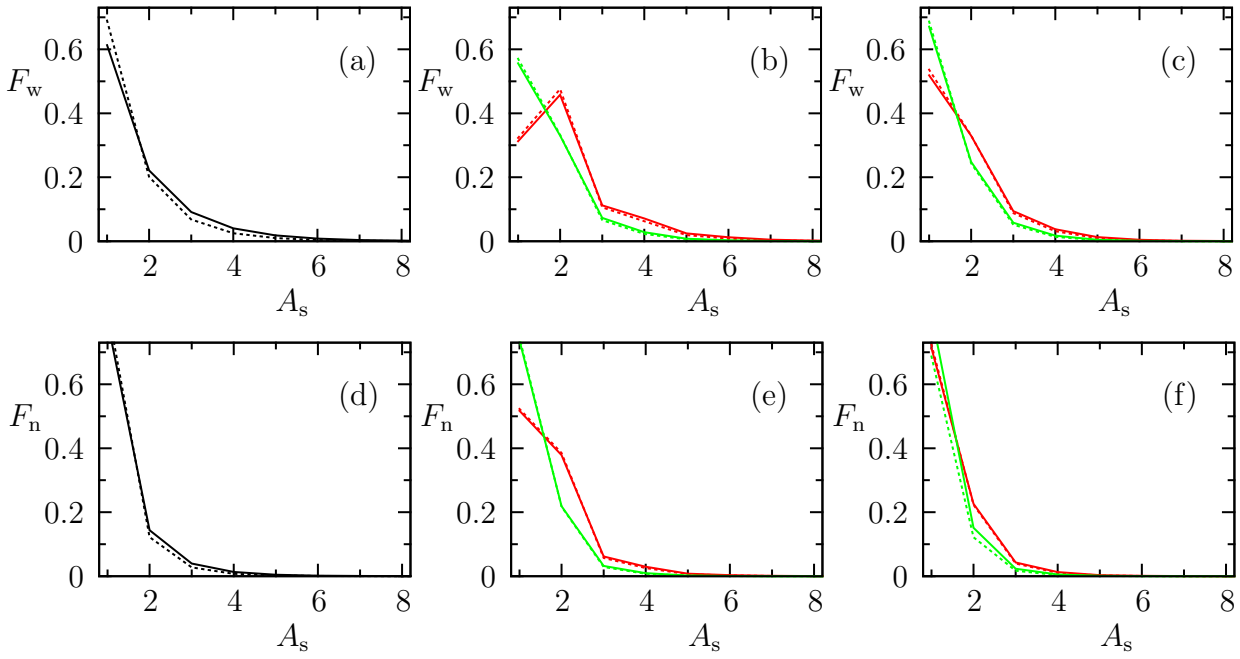

Figure 5.5: Weight distribution function, F_w (figures (a) to (c)), and number distribution function, F_n (figures (d) to (f)), of aggregation numbers, A_s, for double-hydrophilic systems ($a_{A,S} = a_{B,S} = a_{A,CI} = a_{B,CI} = 25$). Figures (a) and (d) show the neutral system, (b) and (e) the charged system with the number of counterions corresponding to the number of A beads, (c) and (f) the charged system with 5 vol% of salt added. Full lines represent systems with compatible blocks ($a_{A,B} = 25$) and dotted lines systems with incompatible blocks ($a_{A,B} = 37.5$), while the red lines are simulations with charge smearing $\lambda_e = 0.2$ and the green ones with $\lambda_e = 0.67$.

(in some cases the dotted and full lines in Figure 5.5 overlap completely), because the diblock as a whole is well soluble.

Next, the results for systems with slightly solvophobic A-blocks ($a_{A,S} = 32.5$) are presented. Figure 5.6 shows the weight distribution functions, $F_w(A_s)$, for systems with fully compatible blocks ($a_{A,B} = 25$), slightly incompatible blocks ($a_{A,B} = 32.5$) and highly incompatible blocks ($a_{A,B} = 37.5$). The weight distributions for neutral systems (Figures 5.6a, 5.6d and 5.6g) are monotonously decreasing curves and the number of non-aggregated chains prevails, but the fraction of low aggregates is not negligible. This suggests the conditions are near the onset of the self-assembling process.

The electrostatic interactions promote the formation of larger aggregates. There is a preference for aggregates with even number of copolymer chains, i.e. the same number of positive $A_5^+B_5$ and negative $A_5^-B_5$ chains, to minimize its electrostatic energy.

Adding salt to the system reduces the fraction of the large aggregates and the difference between aggregates with odd and even aggregation numbers. This is also in accordance with expectations and experimental knowledge. The difference between the system with and without salt (i.e., the second and third column of Figure 5.6) is

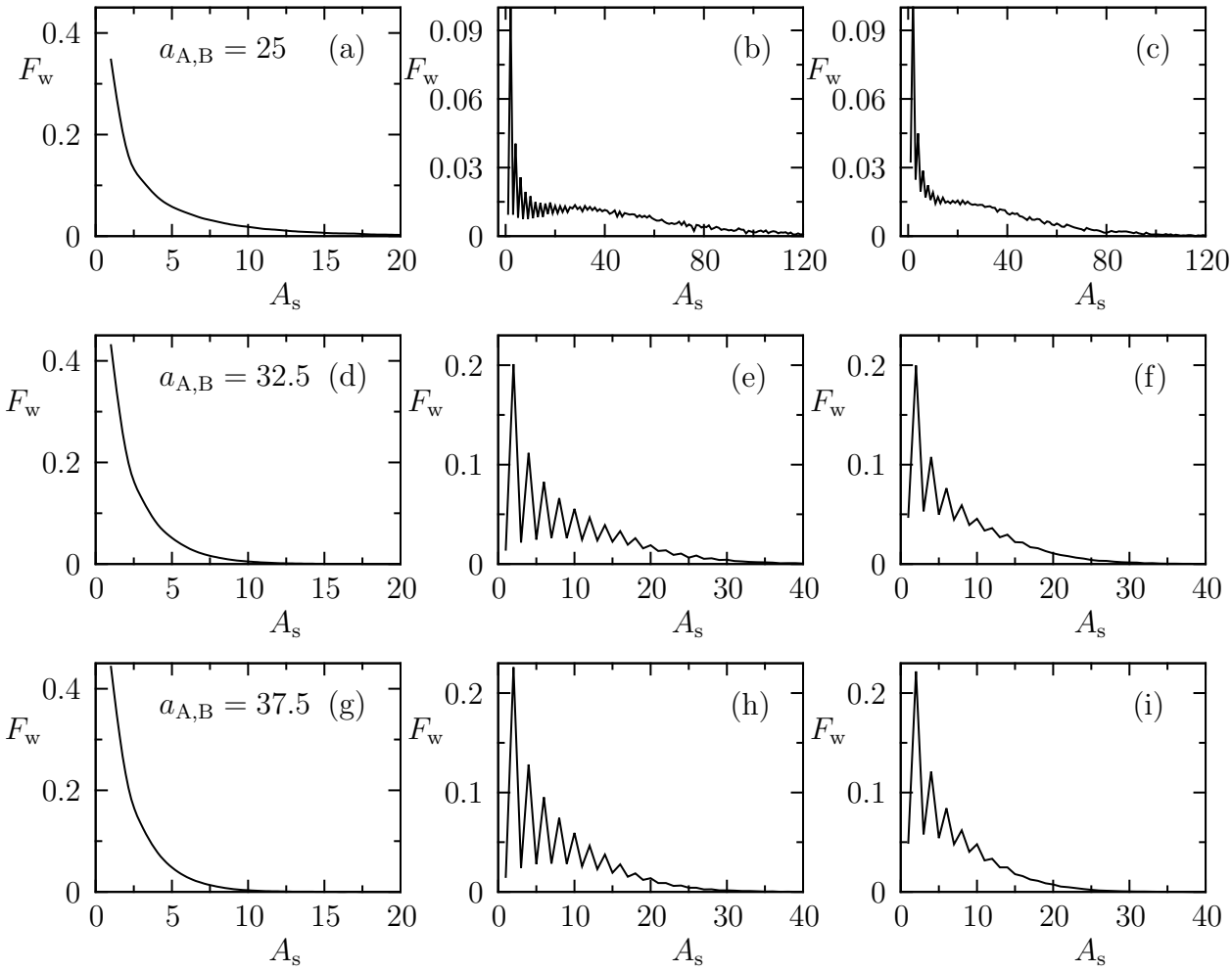

Figure 5.6: Weight distribution functions, F_w, for slightly selective solvent ($a_{A,S} = a_{A,CI} = 32.5$; $a_{B,S} = a_{B,CI} = 25$). Figures (a), (b) and (c) show results for systems with fully compatible blocks ($a_{A,B} = 25$) for neutral system, charged system without salt and charged system with 5 vol% of salt added, respectively. Figures (d), (e) and (f) correspond to slightly incompatible blocks ($a_{A,B} = 32.5$) for the neutral and both charged systems. Figures (g), (h) and (i) are results for highly incompatible blocks ($a_{A,B} = 37.5$) again for all the three systems.

relatively small which is presumably due to the fact the counterions are incompatible with A-blocks and therefore they tend to stay in the bulk solution. Later in this work the comparison between the counterions compatible and incompatible with A beads is presented.

It is interesting to compare the copolymer systems with compatible and incompatible blocks. The weight distribution functions of the two charged systems with compatible blocks in Figures 5.6b and 5.6c show that aggregates up to the aggregation number of about $A_s = 100$ exist in the solution. The comparison of structure of small

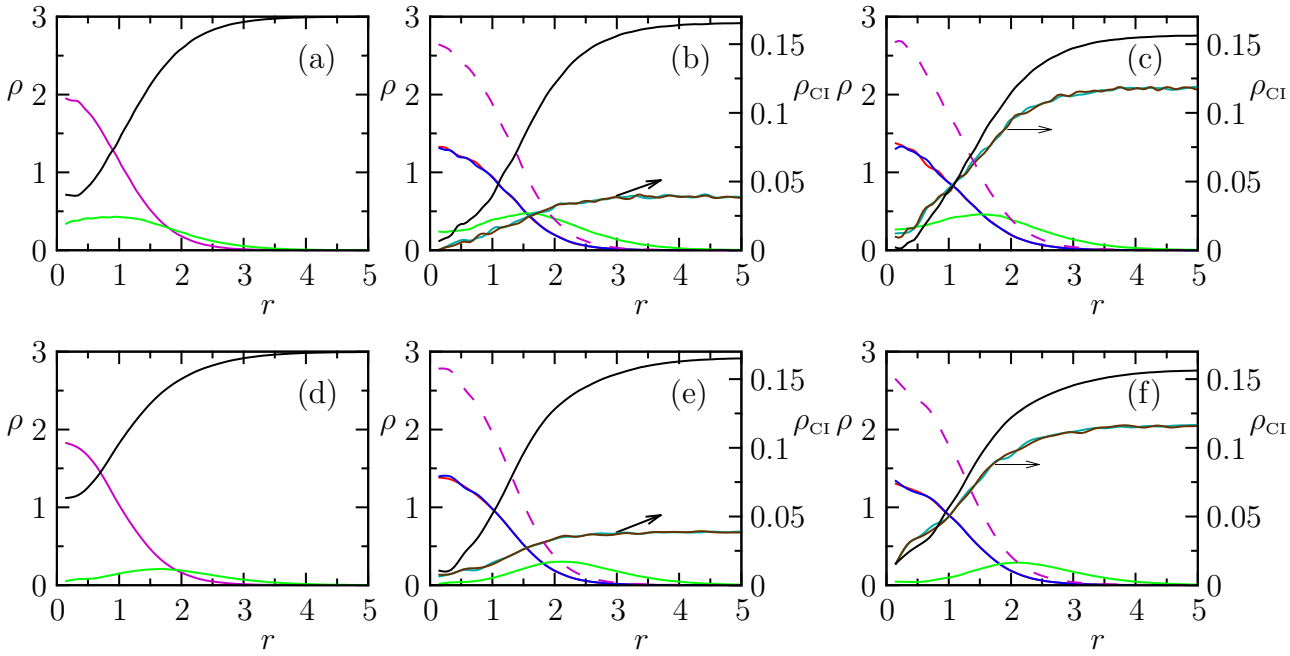

Figure 5.7: Bead density, $\rho(r)$, from aggregates' center of mass for $A_s = 5$ (neutral systems in (a) and (d)) and $A_s = 10$ (charged systems in the remaining figures) in a marginally selective solvent ($a_{A,S} = a_{A,CI} = 32.5$ and $a_{B,S} = a_{B,CI} = 25$). The upper row of figures (a), (b) and (c) shows the results for the systems with compatible blocks ($a_{A,B} = 25$) for the neutral system, the charged system without salt and the charged system with 5 vol% of added salt, respectively. The lower row of figures (d), (e) and (f) corresponds to the systems with highly incompatible blocks ($a_{A,B} = 37.5$) again for the neutral and the two charged systems. A beads are represented by violet lines (neutral systems) or red (A^+ beads) and blue lines (A^- beads), while the violet dashed lines depict the sum of A^+ and A^- beads to compare the cores of charged and neutral aggregates. B beads are green lines; counterions are represented by brown (CI^+) and light blue lines (CI^-); solvent are black lines.

aggregates for systems with compatible and incompatible A and B-blocks is presented in Figure 5.7. The density of all the bead types from the center of mass of an aggregate is depicted there. Figures 5.7a and 5.7d show the densities for neutral aggregates with $A_s = 5$ for compatible and incompatible blocks, respectively. As expected, in the case of compatible blocks the aggregate core is a mixture of A and B particles. On the other hand in the the system with incompatible blocks the core-shell structure is more pronounced. Also more solvent beads are in the core of the aggregate formed by the chains with incompatible blocks. The same tendencies can be observed in charged systems. In all cases the counterions tend to stay outside the aggregate which is understandable, because the core as a whole is neutral and moreover the counterions are incompatible with the A-block as mentioned above.

It should also be noticed the difference between fully compatible blocks and slightly

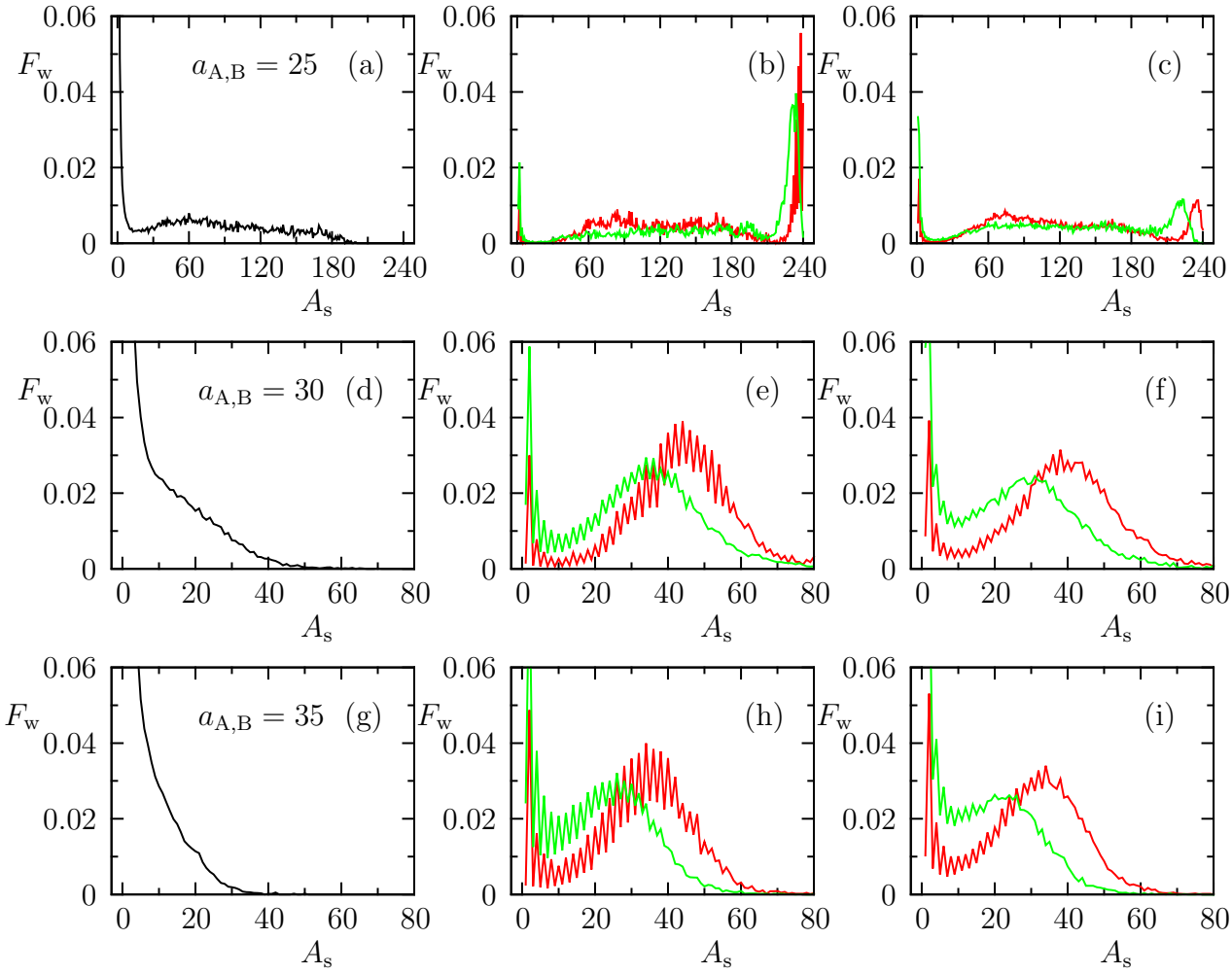

Figure 5.8: Weight distribution functions, F_w, for selective solvent ($a_{A,S} = a_{A,CI} = 35$; $a_{B,S} = a_{B,CI} = 25$). Figures (a), (b) and (c) show the results for the systems with fully compatible blocks ($a_{A,B} = 25$) for the neutral system, the charged system without salt and the charged system with 5 vol% salt added, respectively. Figures (d), (e) and (f) correspond to slightly incompatible blocks ($a_{A,B} = 30$) for the neutral and both charged systems. Figures (g), (h) and (i) are results for more incompatible blocks ($a_{A,B} = 35$) again for all the three systems. Red lines corresponds to the charge smearing of $\lambda_e = 0.2$ and the green ones to $\lambda_e = 0.67$; black lines correspond to neutral systems.

incompatible blocks (i.e., the first and the second row of Figure 5.6) is far more pronounced than that between slighly incompatible and highly incompatible blocks (i.e., the second and the third row of Figure 5.6).

Next, the results for more selective solvent ($a_{A,S} = 35$) are presented and discussed. Figure 5.8 shows the distribution functions for systems with different incompatibilities of A- and B-blocks – the first row shows results for fully compatible blocks ($a_{A,B} = 25$), the second row for slightly incompatible blocks ($a_{A,B} = 30$) and the third row for more

incompatible blocks ($a_{A,B} = 35$). In all cases the same three systems as above are considered – the first column represents the neutral systems, the second column the charged systems with the corresponding number of counterions and the third one the charged systems with 5 vol% of salt added. The weight distributions for systems with both values of charge smearing, $\lambda_e = 0.2$ (red lines) and 0.67 (green lines), are presented for all the charged systems.

In this case considerable aggregation is happening, especially when A and B-blocks are compatible (the upper row of Figure 5.8 with $a_{A,B} = 25$). The weight distribution function for the neutral system (Figure 5.8a) shows the creation of aggregates with sizes of up to ca $A_s = 200$ and for the charged systems all chains may be in one aggregate (Figures 5.8b and 5.8c). This shows that a detailed study of such systems would require much larger simulation box with more diblock chains present. However, the systems are not kinetically frozen as can be seen in Figure 5.9, where the fluctuations of the weight-average aggregation number during the simulation is plotted for the neutral and charged system (for distribution functions in Figures 5.8a and 5.8b). Figure 5.9a shows the neutral system fluctuates fast and randomly, so the simulation yields well equilibrated data. In the Figure 5.9b, there are slower fluctuations, but these are quite large and random. These slower fluctuations suggest the aggregates are more stable then in the neutral system and the exchange of chains between them is less frequent. The upper part of this figure is cut, because the aggregate size is limited by the number of chains in the simulation box. The large fluctuations show that aggregates with quite wide range of A_s coexist in the system.

Figure 5.10 depicts four snapshots of the simulation box for the charged system with $a_{A,S} = 35$ and $a_{A,B} = 25$, i.e. the same systems as in Figures 5.8b and 5.9b. The coexistence of smaller aggregates as well as an aggregate composed of all 240 chains can

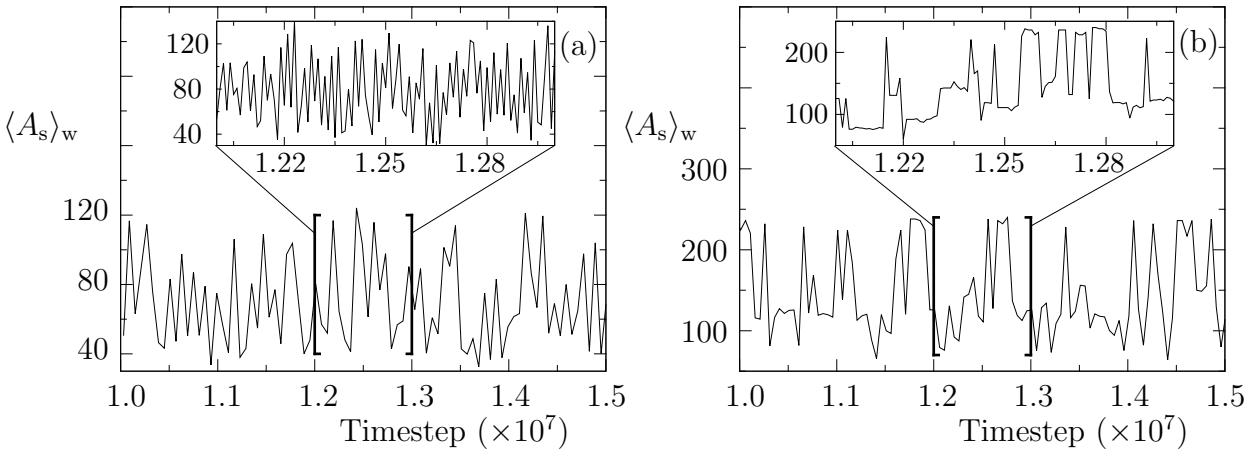

Figure 5.9: Fluctuations of the weight-average aggregation number, $\langle A_s \rangle_w$, in (a) neutral and (b) charged system with $a_{A,S} = a_{A,CI} = 35$ and $a_{A,B} = a_{B,S} = a_{B,CI} = 25$ in equilibrated state.

be seen there. Figure 5.10a and 5.10b show the coexistence of several similarly sized, roughly spherical aggregates with several single chains. Figure 5.10c depicts one small spherical aggregate with one large prolonged and curved aggregate. The last figure shows an aggregate comprised of all the chains in the simulation box. The soluble B-blocks form only a thin layer to protect the insoluble A-blocks from solvent particles, because there is no preference for the B-S interaction over the A-B interaction and therefore B-blocks are also present in the aggregate core.

Structure of several typical aggregates with $A_s \approx 100$ and their comparison between the ones with neutral and charged cores is depicted in Figures 5.11 (neutral system) and 5.12 (charged system). It shows that large aggregates of various shapes (roughly spherical, prolonged, curved and even vesicle-like) coexist with the smaller aggregates. Comparing the neutral and charged aggregates we see the charged ones have cores composed of A beads only partly intermixed with the soluble B beads, while the neutral aggregates have more intermixed A and B-blocks. In all cases the B-blocks form only a thin shell around the aggregate core, but the number of B beads on the outside of the core is visibly higher for the charged aggregates.

These observations are supported by Figure 5.13, where density profiles for the aggregates with $A_s = 100$ are depicted for both neutral (Figure 5.13a) and the two charged systems (Figures 5.13b and 5.13c). The larger compactness of the core of the charged aggregates is demonstrated by the value of reduced density in the aggregate centre $\rho(0) \approx 2.5$ and 2.0 for the charged systems without and with added salt, re-

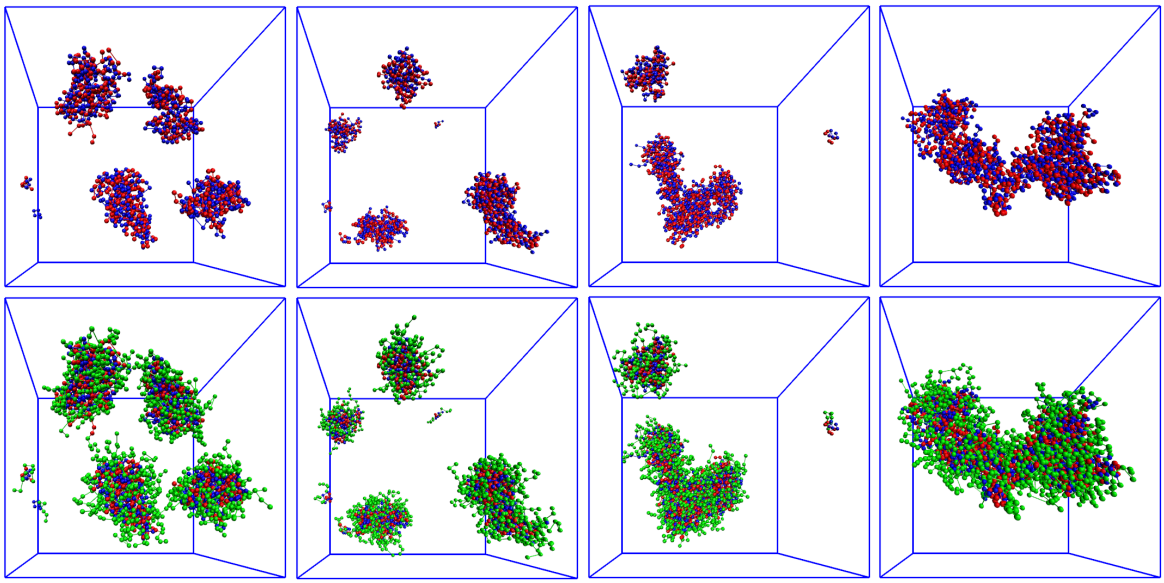

(a) (b) (c) (d)

Figure 5.10: Typical snapshots of the simulation box for charged system without salt with $a_{A,S} = 35$ and $a_{A,B} = a_{B,S} = 25$. Upper row shows only charged A^+ and A^--blocks, while in the lower row the green beads correspond to the well soluble B-blocks.

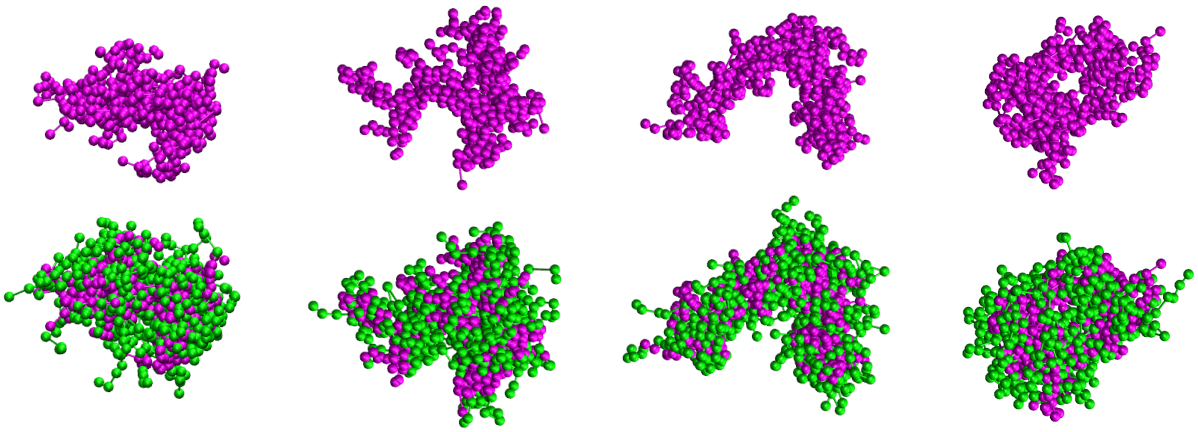

(a) (b) (c) (d)

Figure 5.11: Typical snapshots of aggregates with $A_s \approx 100$ for the neutral system with $a_{A,S} = 35$ and $a_{A,B} = a_{B,S} = 25$. The violet beads represent insoluble A beads and the green ones are soluble B beads.

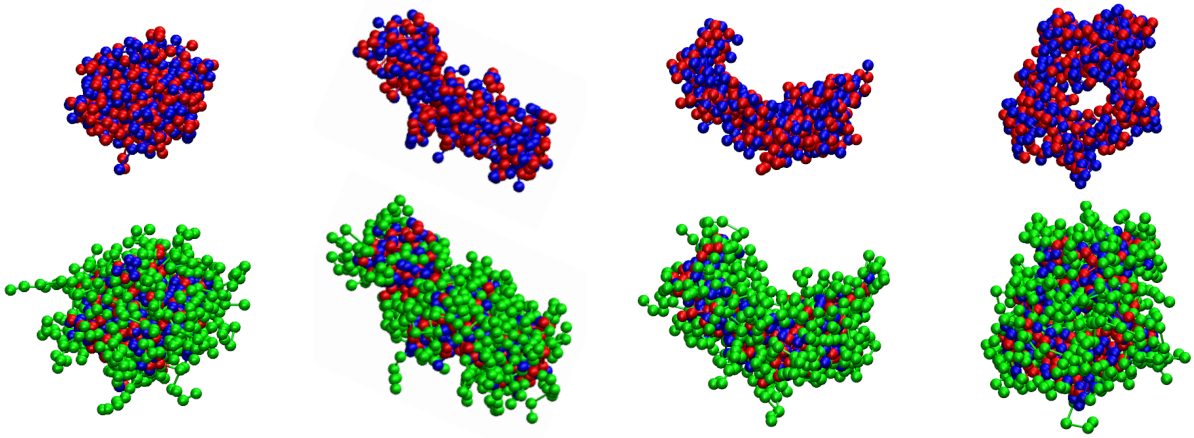

(a) (b) (c) (d)

Figure 5.12: Typical snapshots of aggregates with $A_s \approx 100$ for the charged system with $a_{A,S} = 35$ and $a_{A,B} = a_{B,S} = 25$. The red and blue beads represent insoluble positively or negatively charged A beads, respectively, and the green ones are soluble B beads.

spectively, as opposed to $\rho(0) \approx 1.5$ for the neutral system. In the case of the charged system with added salt (5.13c), there is more small ions and solvent particles present in the core as compared to the system without the salt (5.13b). However, caution must be taken with these observations, because the density profiles are averaged over all aggregate shapes shown in Figures 5.11 and 5.12.

The hydrophobicity of the A-block in the systems with compatible A and B-blocks

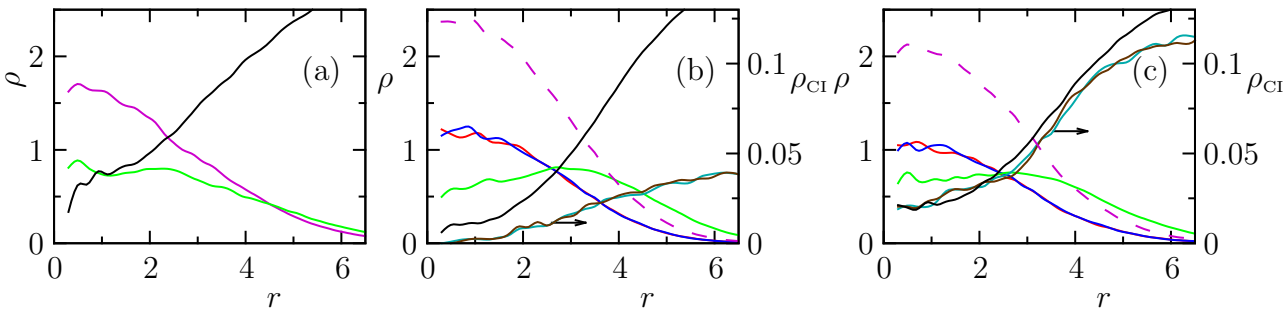

Figure 5.13: Bead density, $\rho(r)$, from aggregate center of mass for $A_s = 100$ in a selective solvent ($a_{A,S} = a_{A,CI} = 35$ and $a_{B,S} = a_{B,CI} = 25$) for compatible A and B-blocks ($a_{A,B} = 25$). Figure (a) shows neutral system, figure (b) charged system without salt and figure (c) is charged system with 5 vol% of added salt. Line colors are same as in Figure 5.7.

promotes the creation of A-domains with low interface to volume ratio, because the A beads tend to minimize the unfavourable interactions with the solvent. Enthalpy is therefore very important in this case and large aggregates are formed. Also the increase in entropy due to the liberation of small counterions further promotes the aggregation process. Furthermore, the electrostatic energy also requires to be minimal (ideally zero), so aggregates with the same number of diblocks containing positive and negative A-blocks should be preferred.

The behaviour of the systems with incompatible blocks (their weight distributions are depicted in the second and third row of Figure 5.8 for two values of incompatibility, $a_{A,B}$) is quite different. The neutral systems (Figure 5.8d and 5.8g) still show monotously decreasing curves and aggregates with A_s of up to about 40 and 30 for systems with $a_{A,B} = 30$ and $a_{A,B} = 35$, respectively, exist in the solution. Electrostatic interactions tip the balance in favour of aggregation and there are evident peaks in their weight distributions between $A_s = 30$ and 45 for all four systems. Adding salt decreases the preference for aggregates with even A_s and slightly increases the fraction of smaller aggregates.

Two typical snapshots of the simulation box containig the charged system with more incompatible blocks ($a_{A,B} = 35$) are shown in Figure 5.14. The coexistence of several similarly sized and roughly sperical aggregates with dimers and other small aggregates is obvious. Also the B-blocks are extended into the solvent and the aggregates have well-defined core-shell structure.

Figure 5.15 shows density profiles for systems with $a_{A,B} = 35$ for $A_s = 20$ (neutral system) and $A_s = 30$ (charged systems). In all three figures core-shell structure is clearly visible with compact core composed of only A-blocks.

All the results for charged systems with $a_{A,S} = 35$ presented and discussed so far only included systems with the charge smearing of $\lambda_e = 0.2$. However, in the second and third column of Figure 5.8 there are presented the weight distributions for the

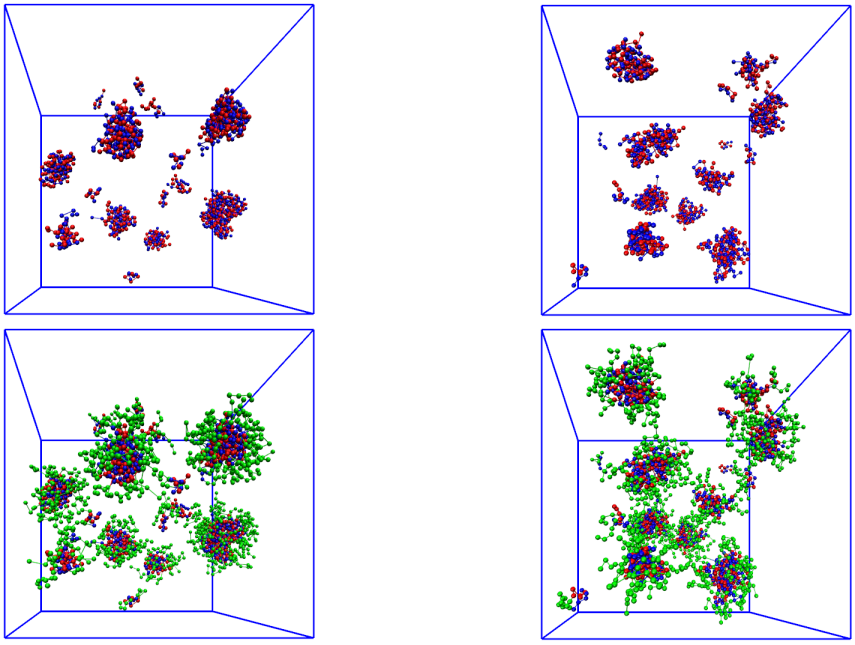

(a) (b)

Figure 5.14: Typical snapshots of the simulation box for charged system without salt with $a_{A,S} = a_{A,B} = 35$ and $a_{B,S} = 25$. Upper row shows only charged A^+ and A^- blocks, while in the lower row the green beads correspond to the well soluble B-blocks.

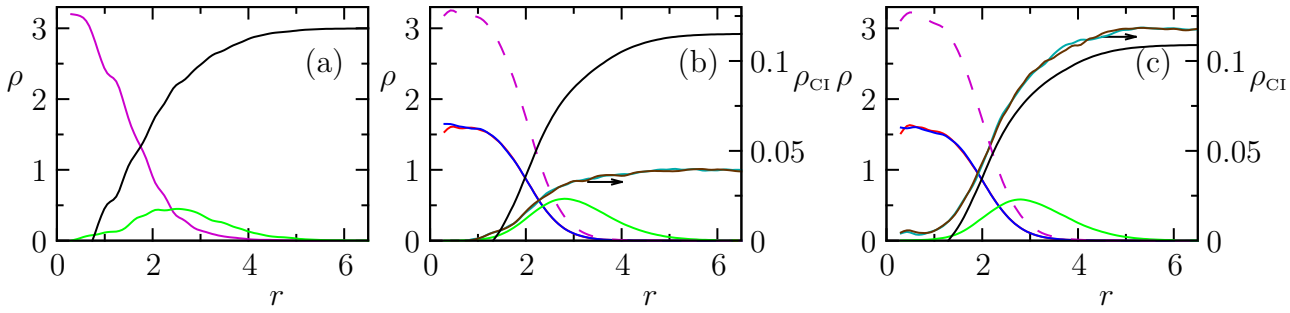

Figure 5.15: Bead density, $\rho(r)$, from aggregate center of mass for $A_s = 20$ (neutral system) and $A_s = 30$ (both charged systems) in a selective solvent ($a_{A,S} = a_{A,B} = a_{A,CI} = 35$ and $a_{B,S} = a_{B,CI} = 25$) for incompatible A and B-blocks ($a_{A,B} = 35$). Figure (a) shows neutral system, figure (b) charged system without salt and figure (c) is charged system with 5 vol% of added salt. Line colors are same as in Figure 5.7.

systems with $\lambda_e = 0.67$ as well (green lines). The difference is relatively large. In all cases, the electrostatic interactions for systems with $\lambda_e = 0.67$ show lesser tendency for aggregation – all green lines are shifted towards lower values of A_s and larger fractions of smaller aggregates are present in the simulations. However, the tendencies are the

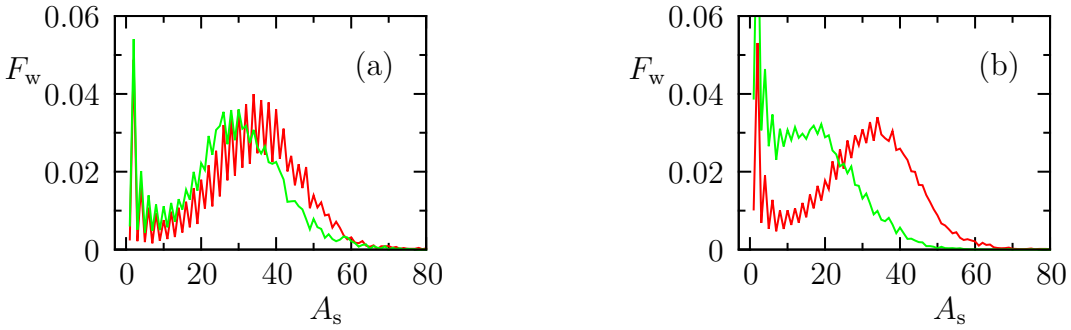

Figure 5.16: Weight distribution functions, F_w, for charged systems with $a_{A,S} = a_{A,B} = 35$ and $a_{B,S} = a_{B,CI} = 25$. Figures (a) and (b) show systems without and with added salt, respectively. Red lines represent systems with $a_{A,CI} = 35$ and green lines the ones with $a_{A,CI} = 25$.

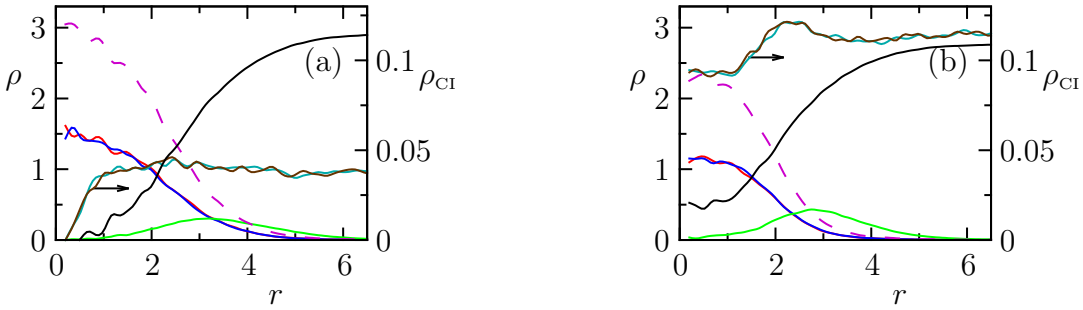

Figure 5.17: Bead density, $\rho(r)$, from aggregate center of mass for $A_s = 30$ in a selective solvent for incompatible A and B-blocks ($a_{A,S} = a_{A,B} = 35$ and $a_{B,S} = a_{B,CI} = 25$) with counterions compatible with A beads ($a_{A,CI} = 25$). Figure (a) charged system without salt and figure (b) is charged system with 5 vol% of added salt. Line colors are same as in Figure 5.7.

same as for the systems with $\lambda_e = 0.2$.

Also, the repulsive parameters of the counterions are the same as that of the solvent particles, therefore A beads are incompatible with the small ions. The effect of this compatibility for the systems with $a_{A,S} = a_{A,B} = 35$ is shown in Figure 5.16, where the weight distribution functions for small ions incompatible with A-blocks ($a_{A,CI} = 35$; red lines) and compatible with A-blocks ($a_{A,CI} = 25$; green lines) for the charged systems without (5.16a) and with added salt (5.16b) are presented. In the case of compatible ions, these beads penetrate the A-domains of the aggregates, partially compensating the charges on the A-blocks. This suppresses the aggregation of PE chains and reduced the preference for even aggregation numbers. Adding salt affects more the system with compatible ions, which is understandable, since more ions penetrate the aggregate core.

The effect of ions compatible with A beads on the aggregate structure is shown in Figure 5.17, where the density profiles for aggregates with $A_s = 30$ for the charged systems without and with salt are depicted. There we see more of small ions and

solvent beads in the aggregate core then in Figures 5.15b and 5.15c, where systems with $a_{A,CI} = 35$ are presented. This makes the core-shell structure of the aggregates less pronounced.

The last section describes the results for highly selective solvent, $a_{A,S} = a_{A,CI} = 37.5$ and $a_{B,S} = a_{B,CI} = 25$. Figure 5.18 shows the weight distribution functions for the systems with slightly incompatible A and B-blocks ($a_{A,B} = 30$; Figures 5.18a to 5.18c) and highly incompatible A and B-blocks ($a_{A,B} = 37.5$; Figures 5.18d to 5.18f). Result for fully compatible A and B-blocks are not presented, because they mirror the behaviour of the systems with $a_{A,S} = 35$ and $a_{A,B} = 25$, but with even higher preference for large aggregates.

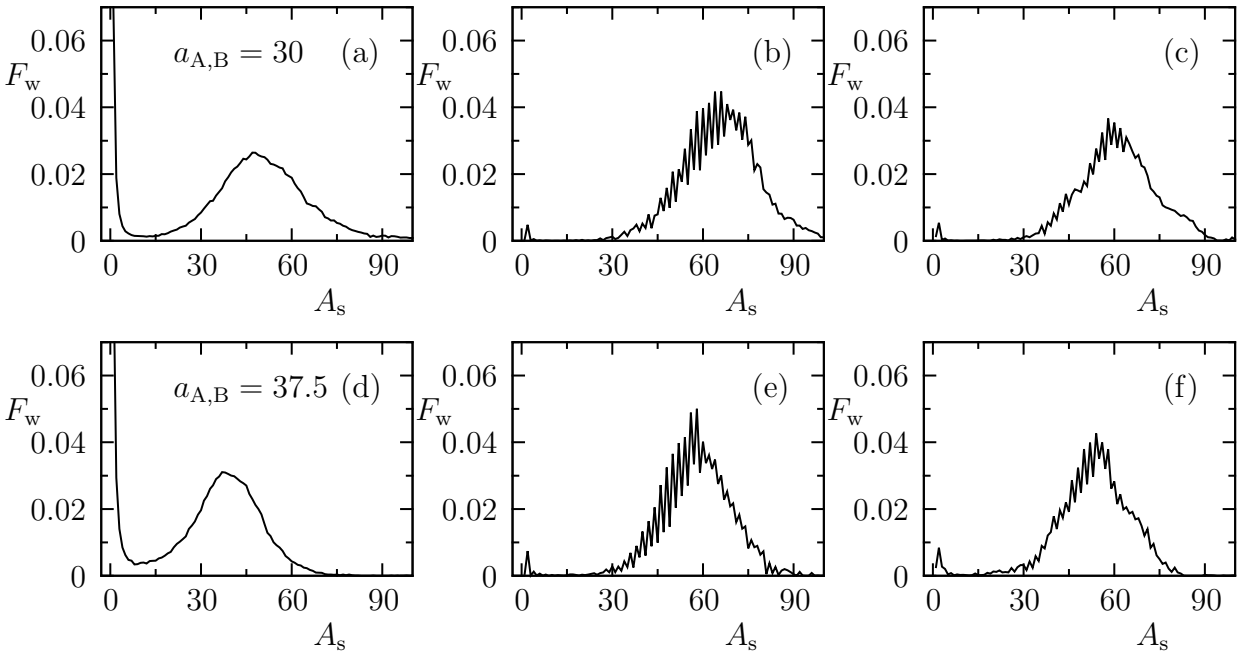

Figure 5.18: Weight distribution functions, F_w, for highly selective solvent ($a_{A,S} = a_{A,CI} = 37.5$; $a_{B,S} = a_{B,CI} = 25$). Figures (a), (b) and (c) show the results for the systems with slightly incompatible blocks ($a_{A,B} = 30$) for the neutral system, the charged system without salt and the charged system with 5 vol% salt added, respectively. Figures (d), (e) and (f) correspond to highly incompatible blocks ($a_{A,B} = 37.5$) for the neutral and both charged systems.

In this highly selective solvent the neutral systems show significant aggregation (Figures 5.18a and 5.18d), but there is still a high fraction of free chains. Electrostatic interactions again promote the self-assembling process, shifting the peak of the weight distributions to higher A_s (Figures 5.18b and 5.18e). Also only a small fraction of aggregates exist outside the larger aggregates (mainly in the form of dimers). Adding salt again has the effect of slightly reducing the fraction of larger aggregates and partly negating the preference for aggregates with even number of chains (Figures 5.18c and 5.18f). Comparing the results for slightly incompatible A and B-blocks (first row of

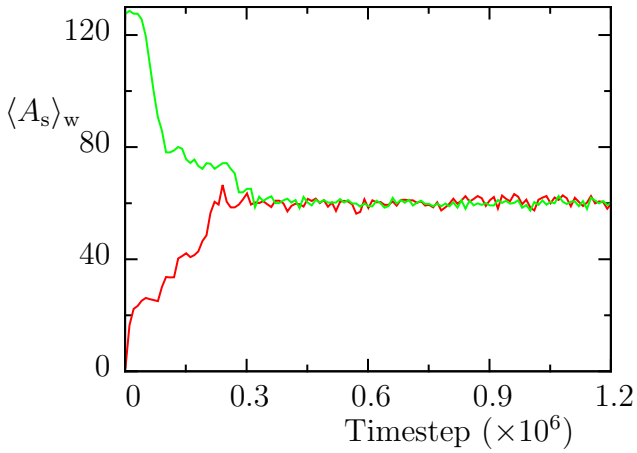

Figure 5.19: Evolution of the weight-average aggregation number, $\langle A_s \rangle_w$, from the beginning of simulations for systems with different starting configurations. Red line shows system with dissolved starting configuration and the green one system starting highly aggregated state.

Figure 5.18) and highly incompatible A and B-blocks (second row of the figure) we can see that increasing the incompatibility forces the weight distribution to slightly lower A_s.

Lastly a proof of the ergodicity of the simulations is given. For the charged system without added salt with $a_{A,S} = a_{A,B} = 37.5$ and $a_{B,S} = 25$ two simulations were performed. One started from a random configuration, where all chains were dissolved, and the second was started from highly aggregated state containing only two large aggregates. Figure 5.19 shows the evolution of the average aggregation number from the simulation beginning for both systems. It is obvious that at the simulation timestep of approximately $3 \cdot 10^5$ the two lines converge. Therefore the simulations are not in any local minimum, because greatly different starting configurations give the same results.

6. Conclusion

The electrostatic co-assembly of equimolar mixtures of oppositely charged symmetric block PEs with one PE block (either strong polycation or strong polyanion) and one readily water-soluble neutral block in aqueous media was studied via the DPD simulation method. In our model, the interactions of the neutral block with the aqueous solvent are always good, but those of the neutral PE backbone with water and the compatibility of the blocks vary in a broad range. The Coulomb interactions between the DPD units were described by the electrostatic potentials between the exponentially smeared elementary charges delocalized exclusively inside the DPD units. The results were compared with those for corresponding neutral systems to obtain information on the roles of all the relevant effects (electrostatics, amphiphilicity of the neutral analogous system and incompatibility of the blocks) and on their intricate interplay.

Copolymers with a highly soluble neutral B-block and a PE A-block which contains a highly soluble neutral backbone electrostatically co-assemble, but do not form large aggregates. Only dimers are formed, because the segments of the A^+/A^--domains interacts favourably with water irrespectively of the overall charge. The process is both entropy-driven and entropy-controlled, but the contributions driving and controlling it are different. The main driving force reflects the appreciable entropy increase due to the liberation of small counterions in the bulk solvent upon the formation of dimers and mutual compensation of opposite charges on the different chains forming the dimer. The controlling term consists of a relatively small entropy decrease due to the aggregation of copolymer chains which is smaller for dimers than for higher aggregates.

The mixtures of copolymers with hydrophobic backbone of the PE A-block (both with A^+ and A^--blocks) and a highly soluble neutral B-block exhibit different assembling behaviour. For incompatible A and B-blocks, multimolecular core-shell aggregates are formed in agreement with the results of a number of experimental studies. The driving force consists of two contributions. The enthalpy contribution reflects minimization of the number of unfavourable interactions of A segments with water due to the formation of compact spherical cores with minimum interface-to-volume ratio. The entropy contribution is caused by the liberation of counterions analogously to the previously discussed case. The aggregation number and size of the aggregates are controlled by a complex interplay of several contributions mostly of entropic origin, similarly to neutral amphiphilic copolymers in selective solvents. The presence of opposite charges on different chains promotes the assembling process. The density of the insoluble do-

mains is higher due to the electrostatic attraction between A^+ and A^- beads and also due to the cooperative effect of multiple charges on the flexible polyions. Both the average aggregation number and the fraction of aggregates increse, but the increase in the former is relatively small compared with the average aggregation number of the neutral system.

The compatibility of the A and B-blocks together with bad solvent quality for the A-block promotes the intermixing of the two copolymer blocks and results in the formation of large microgel-like structures. Opposite electric charges on the A segments suppress the intermixing of A and B segments, because they strengthen the atttractive interaction between two A segments relative to A-B interaction.

Acknowledgment

This work was supported by the Czech Science Foundation, grants P106-12-0143 and P106-13-02938P.

The computing time was provided by MetaCentrum and Cerit-SC.

Access to computing and storage facilities owned by parties and projects contributing to the National Grid Infrastructure MetaCentrum, provided under the programme "Projects of Large Infrastructure for Research, Development, and Innovations" (LM2010005), is greatly appreciated.

Access to the CERIT-SC computing and storage facilities provided under the programme Center CERIT Scientific Cloud, part of the Operational Program Research and Development for Innovations, reg. no. CZ. 1.05/3.2.00/08.0144, is greatly appreciated.

Bibliography

[1] Rubinstein, M.; Colby, R. H.: *Polymer physics.* Oxford University Press (2003).

[2] de Gennes, P. G.: *Scaling concepts in polymer physics.* Cornell university press (1979).

[3] Fujiwara, S.; Itoh, T.; Hashimoto, M.; Horiuchi, H.: *Molecular dynamics simulation of amphiphilic molecules in solution: Micelle formation and dynamic coexistence.* J. Chem. Phys. 130, 144901 (2009).

[4] Forster, S.; Schmidt, M.: *Polyelectrolytes in solution.* Adv. Polym. Sci. 120, 51 (1995).

[5] Dobrynin, A. V.; Rubinstein, M.: *Theory of polyelectrolytes in solutions and at surfaces.* Prog. Polym. Sci. 30, 1049 (2005).

[6] Lindman, B.; Alexandridis, P.: *Amphiphilic block copolymers: Self-assembly and applications.* Elsevier Science (2000).

[7] Alexander, S.; Chaikin, P. M.; Morales, G. J.; Grant, P.; Pincus, P.; Hone, D: *Charge renormalization, osmotic pressure, and bulk modulus of colloidal crystals: Theory.* J. Chem. Phys. 80, 5776 (1984).

[8] Wong, G. C. L.; Pollack, L: *Electrostatics of strongly charged biological polymers: Ion-mediated interactions and self-organization in nucleic acids and proteins.* Annu. Rev. Phys. Chem. 61, 171 (2010).

[9] Manning, G. S.: *Limiting laws and counterion condensation in polyelectrolyte solutions.* J. Chem. Phys. 51, 924 (1969).

[10] Gillespie, D. A. J.; Hallett, J. E.; Elujoba, O.; Hamzah, A. F. C.; Richardson, R. M.; Bartlett, P.: *Counterion condensation on spheres in the salt-free limit.* Soft Matter 10, 566 (2014).

[11] Manning, G. S.: *Counterion condensation theory constructed from different models.* Physica A 231, 236 (1996).

[12] Moritz, R.; Zardalidis, G.; Butt, H.-J.; Wagner, M.; Müllen, K.; Floudas, G.: *Ion size approaching the Bjerrum length in solvents of low polarity by dendritic encapsulation.* Macromolecules 47, 191 (2014).

[13] Chennamsetty, N.; Bock, H.; Lísal, M; Brennan, J. K.: *An introduction to coarse-graining approaches: Linking atomistic and mesoscales.* Molecular Systems Engineering (2011).

[14] Muller-Plathe, F.: *Coarse-graining in polymer simulation: From the atomistic to the mesoscopic scale and back.* Chem. Phys. Chem. 3, 754 (2002).

[15] Ortiz, V.; Nielsen, S. O.; Klein, M. L.; Discher, D. E.: *Computer simulation of aqueous block copolymer assemblies: Length scales and methods.* J. Polym. Sci. B Polym. Phys. 44, 1907 (2006).

[16] Carbone, P.; Varzaneh, H. A. K.; Chen, X.; Müller-Plathe, F.: *Transferability of coarse-grained force fields: The polymer case.* J. Chem. Phys. 128, 064904 (2008).

[17] Izvekov, S.; Parrinello, M.; Burnham, C. J.; Voth, G. A.: *Effective force fields for condensed phase systems from ab initio molecular dynamics simulation: A new method for force-matching.* J. Chem. Phys. 120, 10896 (2004).

[18] Izvekov, S.; Voth, G. A.: *A multiscale coarse-graining method for biomolecular systems.* J. Chem. Phys. B 109, 2469 (2005).

[19] Groot, R. D.; Warren, P. B.: *Dissipative particle dynamics: Bridging the gap between atomistic and mesoscopic simulation.* J. Chem. Phys. 107, 4423 (1997).

[20] Spenley N. A.: *Scaling laws for polymers in dissipative particle dynamics.* Europhys. Lett., 49, 534 (2000).

[21] Maiti, A.; McGrother, S.: *Bead-bead interaction parameters in dissipative particle dynamics: Relation to bead-size, solubility parameter, and surface tension.* J. Chem. Phys. 120, 1594 (2004).

[22] Frenkel, D.; Smit, B.: *Understanding molecular simulation.* Academic Press, New York (1996).

[23] Español, P.: *Dissipative particle dynamics revisited.* Challenges in Molecular Simulations, 59 (2002).

[24] Glotzer, S. C.; Paul, W.: *Molecular and mesoscale simulation methods for polymer materials.* Annual review of materials research 32, 401 (2002).

[25] Español, P.; Warren, P.: *Statistical mechanics of dissipative particle dynamics.* Europhys. Lett. 30, 191 (1995).

[26] Gai, J. G.; Hu, G. H.; Li, H. L.; Zhu, S. P.; Hoppe, S.: *Dissipative particle dynamics and Flory-Huggins theories for predicting the rheological behavior of ultrahigh molecular weight olyethylene blends.* Ind. Eng. Chem. Res. 49, 11369 (2010).

[27] Nikunen, P.; Karttunen, M.; Vattulainen, I.: *How would you integrate the equations of motion in dissipative particle dynamics simulations?.* Comp. Phys. Communications 53 (2003).

[28] González-Melchor, M.; Velázquez, E. M.; Velázquez, M. W.; Alejandre, J.: *Electrostatic interactions in dissipative particle dynamics using Ewald sums.* J. Chem. Phys. 125, 224107 (2006).

[29] Toukmaji, A. Y.; Board, J. A.: *Ewald summation techniques in perspective: a survey.* Comp. Phys. Communications 95 (1996).

[30] Groot, R. D.: *Electrostatic interactions in dissipative particle dynamics – simulations of polyelectrolytes and anionic surfactants.* J. Chem. Phys. 118, 11265 (2003).

[31] Posel, Z.; Limpouchová, Z.; Šindelka, K.; Lísal, M.; Procházka, K.: *Dissipative particle dynamics study of pH-dependant behavior of poly(2-vinylpyridine)-block-poly(ethylene oxide) diblock copolymer in aqueous buffers.* Macromolecules 47, 2503 (2014).

[32] Beckers, V. L.; Lowe, C. P.; de Leeuw, S. W.: *An iterative PPPM method for simulating coulombic systems on distributed memory parallel computers.* Mol. Simul. 20, 369 (1998).

[33] Warren, P. B.; Vlasov, A.; Anton, L.; Masters, A. J.: *Screening properties of Gaussian electrolyte models, with application to dissipative particle dynamics.* J. Chem. Phys. 138, 204907 (2013).

[34] Saint-Martin, H.; Hernández-Cobos, J.; Bernal-Uruchurtu, M. I.; Ortega-Blake, I.; Berendsen, H. J. C.: *A mobile charge densities in harmonic oscillators (MCDHO) molecular model for numerical simulations: The water–water interaction.* J. Chem. Phys. 113, 10899 (2000).

[35] Groot, R. D.; Rabone, K. L.: *Mesoscopic simulation of cell membrane damage, morphology change and rupture by nonionic surfactants.* Biophys. J. 81, 725 (2001).

[36] Soto-Figueroa, C.; Vicente, L.; Martinéz-Magadán, J.-M.; Rodríguez-Higaldo, M.: *Self-organization process of ordered structures in linear and star poly(styrene)-poly(isoprene) block copolymers: Gaussian models and mesoscopic parameters of polymeric systems.* J. Chem. Phys. B 111, 11756 (2007).

[37] Guo, H.; Qiu, X.; Zhou, J.: *Self-assembled core-shell and Janus microphase separated structures of polymer blends in aqueous solution.* J. Chem. Phys. 139, 084907 (2013).

[38] Seaton, M.A.;. Anderson, R.L.; Metz, S.; Smith, W.: *DL_MESO: Highly scalable mesoscale simulations.* Mol. Sim. 39, 796 (2013).

[39] Theodorou D. N., Suter U. W.: *Shape of unperturbed linear polymers: polypropylene.* Macromolecules 18, 1206 (1985).

[40] Newkome G. R., Moorefield C. N., Vogtle F.: *Dendrimers and dendrons: Concepts, syntheses, applications.* Wiley-VCH, Weinhim (2004).

[41] Cheng L., Cao D.: *Effect of tail architecture on self-assembly of amphiphiles of polymeric micelles.* Langmuir, 25, 2749 (2009).

[42] Binder, K.: *Monte Carlo and molecular dynamics in polymer science.* Oxford university press (1995).